

On the link between fracture toughness, tensile strength, and fracture process zone in anisotropic rocks



Nathan Dutler^a, Morteza Nejati^{b,*}, Benoît Valley^a, Florian Amann^c, Giulio Molinari^d

^a Center for Hydrogeology and Geothermics, University of Neuchâtel, Neuchâtel, Switzerland

^b Department of Earth Sciences, ETH Zurich, Switzerland

^c Chair of Engineering Geology and Environmental Management, RWTH Aachen, Germany

^d Laboratory of Composite Materials and Adaptive Structures, Department of Mechanical and Process engineering, ETH Zurich, Switzerland

ARTICLE INFO

Keywords:

Fracture toughness anisotropy
Strength anisotropy
Fracture process zone
Digital image correlation
Transverse isotropy

ABSTRACT

This paper presents experimental results on the anisotropy of the fracture toughness, Brazilian tensile strength, and the fracture process zone (FPZ) in granodiorite samples. The fracture toughness is measured using semi-circular bending tests, while Brazilian disk tests were conducted to measure the tensile strength indirectly. Digital image correlation (DIC) was employed to obtain full-field surface deformation associated with the fracture propagation and identify the FPZ. An averaging scheme is proposed to determine the length and width of the FPZ from the strain field. The DIC results confirm a semi-elliptical FPZ developing ahead of the crack tip, with an average length-to-width ratio of approximately two. The results also indicate that the theoretical models such as Irwin and strip-yield with uniform traction, which are based on plastic deformation near the crack tip, underestimate the extent of the inelastic zone, while the strip-yield model with a linear cohesion stress distribution overestimate the length of the process zone. The anisotropy ratio of the FPZ length obtained from the models, however, agrees very well with the ratio obtained from the DIC measurements. This evidence supports the basis of the theoretical models that predict the FPZ length to be proportional to the square of fracture toughness over tensile strength.

1. Introduction

The mechanics of crack growth in rocks is an important field of research with direct applications in many geoscience and geoenvironmental fields including geothermal energy production, mining, tunneling, earthquake seismology, and reservoir geomechanics. In order to analyse the mechanics of fracturing in rocks, mechanical properties such as elasticity constants, strength and fracture toughness have to be accurately measured. An example of the importance of the anisotropy in rock mass response to external loading was recently demonstrated in an in-situ stimulation and circulation project in the deep underground laboratory at the Grimsel Test Site in Switzerland [1–3]. Elasticity parameters characterize the elastic deformation of rock due to the applied load, while strength is the critical tensile or compressive stress at which the rock fails. Closely related to the strength is a parameter called fracture toughness which is a measure of the resistance of rock against crack growth. Fracture toughness is a key intrinsic material property used in analyzing brittle fracture growth.

Due to the texture or layered structure developed during the formation or metamorphic process (e.g. foliation, bedding), a large

* Corresponding author.

E-mail address: mnejati@ethz.ch (M. Nejati).

<https://doi.org/10.1016/j.engfracmech.2018.08.017>

Received 11 May 2018; Received in revised form 27 July 2018; Accepted 10 August 2018

Available online 23 August 2018

0013-7944/ © 2018 Elsevier Ltd. All rights reserved.

Nomenclature			
α	dimensionless crack length	S	span length
a	initial crack length	S_{ij}	compliance matrix component ij
B	specimen thickness	σ_t	tensile strength
D	SCB and BD diameter	σ_t^{iso}	tensile strength calculated based on isotropic elasticity assumption
E, E'	Young's moduli within and normal to the isotropy plane	σ_u	yield strength
ϵ_{ij}	strain component ij	σ_i	normal stress component in direction i
ϵ_1	maximum principal strain	τ_{ij}	shear stress ij
ϕ	angle between the crack plane and the foliation (isotropy) plane	u, v	Displacements along x and y directions
G, G'	shear moduli within and normal to the plane of isotropy	$\mu_i, \bar{\mu}_i$	conjugate pair of roots to the 4th order characteristic equation of anisotropic elasticity $i = 1, 2$
L	FPZ length	x, y	Cartesian coordinates
K_I	mode I stress intensity factor	Y_I, Y_{II}	normalised stress intensity factors for modes I and II
K_{Ic}	mode I fracture toughness	W	FPZ width
L_f^p, L_s^p	length of the plastic zone by the Irwin's and strip-yield models	Abbreviations	
L_t	length of the process zone estimated from Irwin's model	AE	acoustic emission
L_{Su}, L_{S1}, L_{Sn}	length of the process zone estimated from strip-yield model with uniform, linear and nonlinear cohesion stress variation along the FPZ	BD	Brazilian disk
ν, ν'	Poisson's ratio within and normal to the plane of isotropy	CB	chevron bend
P, P_m	load and peak load	CCNBD	cracked chevron notched Brazilian disc
R	sample radius	DIC	digital image correlation
r, θ	polar coordinates of a point near the crack tip	FPZ	fracture process zone
		GTS	Grimsel Test Site
		ISRM	International Society for Rock Mechanics
		LEFM	linear elastic fracture mechanics
		SCB	semi-circular bend
		SR	short rod

class of rocks have anisotropic mechanical properties such as elasticity, strength and fracture toughness. The anisotropy of fracture toughness implies the directional-dependency of the rock resistance against crack growth. In the context of linear elastic fracture mechanics, the fracture toughness is closely related to the concept of the fracture energy G_f defined by Griffith. The Griffith theory of fracture growth postulates that the strain energy released due to the fracture growth is consumed to create the fracture surfaces. The process of creating fracture surfaces may involve dissipation of energy by heat, wave propagation, inelastic deformation near the fracture surfaces and bonds breakage between the fracture surface [4,5].

The growth of crack in rocks is accompanied by significant inelastic deformation near the crack tip. This highly damaged region adjacent to the crack tip is called fracture process zone (FPZ) within which the material undergoes micro-damaging. In the fracture process zone, micro-cracks close or open depending on their orientation with respect to the direction of the applied load, and crack growth in fact occurs by connecting the micro-cracks at a critical load. The fracture toughness K_{Ic} gives the intensity of stress at this critical state. One of the reasons for the anisotropy of the fracture toughness and tensile strength is the preferential direction of pre-existing micro-cracks, which seems to be mostly aligned with the textural orientation of rock such as foliation or bedding. Therefore, the interaction of newly developed micro-cracks with the pre-existing ones, in terms of density, size and orientation, is central in understanding the anisotropy of the fracture toughness [6].

The anisotropic elasticity of foliated and sedimentary rocks can be efficiently modeled through a transversely isotropic constitutive behavior which includes five elastic constants in the model. This approximation relies on the fact that there is an isotropic plane normal to which a different Young's modulus is to be expected. The isotropy plane is often assumed to be the foliation or bedding plane of the rock. Apart from the elasticity, strength and toughness are also expected to be anisotropic and dependent on the direction of the applied load with respect to the plane of anisotropy. Most of the studies conducted on the anisotropy of fracture toughness focus on the anisotropic ratio and its correlation with the micro-crack structure of rock (see a review in Section 2). However, a key ingredient of fracturing is the fracture process zone (FPZ), and the development and characteristics of this zone in anisotropic rocks have not been investigated so far. Most of research on FPZ development is focused on concrete, and occasionally on some isotropic rocks. It is well known that the FPZ has a central role in linking the fracture toughness and strength.

This work investigates the anisotropy of the tensile strength and mode I fracture toughness in granodiorite samples from Grimsel Test Site (GTS) in Switzerland. Digital image correlation (DIC) is employed to observe the development of fracture process zone near the crack tip. An averaging method is used to calculate the width of the FPZ from strain and displacement fields. The size and shape of the FPZ calculated from the DIC results are then used to evaluate the anisotropy of the FPZ. The results show that the FPZ develops as a semi-elliptical localized region, with the ratio of length to width being about two in both principal directions (isotropic shape). However, the actual values of the length and width show slight anisotropy, with the size of the FPZ being bigger for cracks oriented along the foliation compared to the ones oriented normal to the foliation plane. It is also shown that the theoretical models such as

Irwin and strip-yield with uniform traction underestimate the extent of the inelastic zone, while the strip-yield model with a linear cohesion stress distribution overestimate the length of the process zone. However, the ratio of the FPZ lengths at principal directions fits the theoretical models very well. This indicates that the length of the FPZ is indeed proportional to the square of fracture toughness over strength.

2. Fracture toughness and strength

2.1. Fracture toughness measurement

Several methods of measuring mode I fracture toughness exist in literature. Reviews on various methods with their attributes, advantages and drawbacks are given in Whittaker et al. [7] and Bearman [8]. To obtain precise, accurate and consistent results, the International Society for Rock Mechanics (ISRM) recommends four test procedures: (1) Chevron bend (CB) [9]; (2) Short rod (SR) [9]; (3) Cracked chevron notched Brazilian disc (CCNBD) [10]; and (4) Notched semi-circular bend (SCB) [11]. These standards indicate the requirements for the samples in terms of their preparation, dimensions, and test procedure in terms of loading type and rate. Formulae are also provided to calculate the fracture toughness from the failure load and geometrical factors.

Despite standardized testing, the results from CB, SR and CCNBD exhibit a deviation in the range of 20–30%. This deviation is often explained by size effects, anisotropy of the rock and inaccuracy of the dimensionless parameters used in the calculation. Among these methods, the CCNBD show a consistently lower variation [12]. Iqbal and Mohanty [13] compared CB and CCNBD methods on three different rock types with two-hundred specimens and concluded that the methods are very comparable when the correct equation for fracture toughness calculation was used and the specimen size was selected carefully. Kataoka et al. [14] compared CB and SCB method using Kimachi sandstone and obtained almost the same values. In term of size effects, the recommended ISRM procedure for a specific method allows to minimize the variation of fracture toughness values among the different methods.

The effect of rock anisotropy on fracture toughness has been investigated in a number of studies. Krishnan et al. [15] and Ke et al. [16] studied the fracture toughness anisotropy of sandstone and marble using Cracked Straight Through Brazilian Disc (CSTBD) specimens. Kataoka and Obara [17] and Kataoka et al. [18] used the SCB method to study two end-member configurations (named as short-transvers and arrester) of anisotropy in rocks under water-vapor pressure. The CCNBD method was used by Nasser and Mohanty [19] to measure the fracture toughness of different granitic rocks and sandstones at different orientations. Chandler et al. [20] and Chandler et al. [21] used a SR method to study Mancos shale in three configurations arrester, divider and short-transverse, at different temperatures. The SCB method was used by Funatsu et al. [22] to study the relationship between fracture toughness and loading axis with respect to the bedding planes using sandstone.

In this study, the notched semi-circular bend configuration is used for investigating the fracture toughness anisotropy in Grimsel Granodiorite. The advantages of using SCB specimens are (1) it requires small samples, (2) sample preparation is easy due to minimal machining, and (3) only the failure load is required to determine the fracture toughness [11]. The effect of anisotropy can also be studied in a straightforward fashion by using SCB samples. Using this method, it is necessary to use slow loading rates so that the dynamic effects can be ignored.

2.2. Anisotropy of fracture toughness

Table 1 summarizes the findings on the anisotropic fracture toughness in different types of rocks. An important result is the identification of the central role of micro-structure orientation and grain size in the anisotropy of the fracture toughness. The fracture toughness is closely linked to the presence of micro-cracks and their orientation. It is in fact reported that micro-crack structure in crystalline rock is more important than the grain size and orientation when it comes to the fracture toughness [19].

A correlation between the orientation of foliation/bedding and the maximum of P-wave velocity was observed in granite and shale [19,20]. The highest P-wave velocity is measured parallel to foliation/bedding while the minimum value was obtained in the direction normal to the foliation/bedding. This fact indicates that the micro-cracks are dominantly oriented along the foliation/bedding. The reason for lower measured values of fracture toughness along foliation and bedding seems to be the higher density of micro-cracks in those directions. The process of fracture growth is explained by the gradual initiation and growth of (existing) micro-cracks, and their coalescence to form larger cracks. Therefore, higher density and larger micro-cracks facilitates the growth of fracture in certain directions.

The presence of a correlation between fracture toughness and fracture surface roughness of Stanstead and Barre granite was suggested by Nasser et al. [23,24]. Their study shows a significant increase of K_{Ic} and fracture roughness between directions parallel to and normal to petrofabric orientation. In addition, the rock with a coarser micro-structural fabric shows a rougher fracture surface. The results generally confirm an essential link among petrofabric anisotropy, fracture toughness, fracture roughness, and evolution and extent of associated induced cracks along specific directions in the fracture process zone. Similar results have been shown for shale, where the fracture growing normal to the direction of bedding seems to be tortuous and kinked, inducing a rougher fracture surface [20].

2.3. Anisotropy of strength

The tensile strength of brittle materials can be obtained by direct or indirect methods. A simple indirect method is the Brazilian tensile test in which a thin circular disk is loaded diametrically up to failure (see reviews by Li and Wong [25] and Perras and

Diederichs [26]). This diametrical compression induces a tensile stress normal to the direction of applied load, and it is expected that the specimen failure initiates at the point of maximum tensile stress, i.e. at the center of disk. The elasticity solution that calculates the stress at the center of disk is based on a homogeneous, isotropic and linearly elastic material behavior [27–29], and requires only the peak load and sample dimensions to calculate the tensile strength. With the introduction of anisotropic elasticity, the solution is not only a function of loading and geometry dimensions, but also the elastic constants of the anisotropic material. The explicit representation of stress in a Brazilian disk with transversely isotropic material has been given by Chen et al. [30], Exadaktylos and Kaklis [31] and Claesson and Bohlooli [32]. These studies are based on the Lekhnitskiy's anisotropic elasticity solution [33], and show that the elasticity solution of Brazilian disk depends on two material parameters.

The early work of Barla and Innaurato [34] investigated the suitability of Brazilian and ring tests for the measurement of tensile strength. Using finite element simulations, they concluded that the anisotropy has a significant influence on the stress at the center of disk, and therefore the tensile strength measurement based on an isotropic elasticity solution may be significantly inaccurate. They also found that the failure may occur along the bedding or foliation, and not always along the loading direction, which raises serious doubts on the nature of failure process. Many experimental results on anisotropic rocks show that the micro-structure orientation can significantly influence the strength of rock, with the strength along the bedding or foliation is significantly lower than perpendicular to it [35–38]. It has also been shown that when the foliation or bedding is oblique to the direction of applied load, a significant shearing component develops at the plane of failure, which raises doubts on the suitability of the results to be considered as tensile strength.

3. Fracture process zone

This section provides a review on the previous work related to the development of the FPZ in quasi-brittle materials.

3.1. Characteristics of process zone

Linear elastic fracture mechanics describe a square-root singular stress state adjacent to the tip of a sharp crack. However, no material is able to resist an infinite amount of stress, and therefore the material undergoes an inelastic deformation in the vicinity of

Table 1
A summary of findings on the fracture toughness of anisotropic rocks

Rock type	Methodology	Important results	Reference
Sandstone Marble	Notched Brazilian disk specimen Microscopic analysis Mixed mode I/II experiments	<ul style="list-style-type: none"> Mixed-mode I/II fracture envelopes were developed. The effect of anisotropy on fracture toughness can be significant. 	Krishnan et al. [15] and Ke et al. [16]
Granite	Cracked chevron notched Brazilian disk specimen Microscopic analysis Acoustic Emission 3D X-ray and CT scans	<ul style="list-style-type: none"> Micro-crack density and length are major contributors to the value of fracture toughness. Fracture toughness is inversely proportional to micro-crack density and length. There is a correlation between fracture toughness and fracture roughness. FPZ from acoustic emission and optical measurement are in good agreement. The seismic velocities is closely linked to the micro-crack density and its orientation. A decreasing anisotropy was observed with the increase of the loading rate. 	Nasseri et al. [64,68], Nasseri and Mohanty [19], Nasseri et al. [23,24,108] and Dai et al. [109]
Granite	Notched semi-circular bend specimen Acoustic emission Ultrasonic measurements Microscopic analysis 3D X-ray CT scans	<ul style="list-style-type: none"> Orientation of micro-cracks can be estimated by measurement of wave velocity. Both elastic wave velocity and fracture toughness exhibit anisotropy. Fracture toughness is dependent on the micro-structure of rock. K_{Ic} decreases with increasing water vapor pressure. 	Kataoka et al. [18]
Shale	Notched semi-circular bend specimen Microscopic analysis	<ul style="list-style-type: none"> The influence of calcite-filled veins on propagation path is investigated. The propagation is strongly influenced by the approach angle of the induced fracture to the veins and the thickness of the veins. 	Lee et al. [110]
Shale	Short rod specimen Ultrasonic measurements Microscopic analysis	<ul style="list-style-type: none"> Strong fracture toughness anisotropy was observed in shale. K_{Ic} changes very little up to 120 °C at which temperature it starts to increase slightly. When the original crack is oriented normal to the bedding, there is a strong tendency to deviate towards the bedding. 	Chandler et al. [20,21]

the crack tip. This inelastic region is of different nature depending on the material type. Metals often exhibit yielding and plasticity, often accompanied with strain hardening, due to the distortional component of stress. For this reason, the inelastic region near the tip in metals is called the plastic zone. On the other hand, brittle materials often exhibit damage due to initiation and propagation of micro-cracks, which is accompanied with strain softening and mainly driven by normal components of stress. For this reason, the inelastic region in brittle materials is often called fracture process zone (FPZ). In materials such as rock and concrete, the size of the FPZ can be large enough to introduce significant nonlinearity (softening) near the failure point. These materials derive their toughness from subcritical cracking that precedes the ultimate failure. This is the reason to name this types of materials as “quasi-brittle” rather than “brittle”. Both plastic and fracture process zones are regions where considerable energy dissipation occurs. The fracture energy and toughness will therefore depend on the strength of the degree of nonlinearity and the size and shape of these zones.

The FPZ develops as a transition zone between the macro-crack which has strong discontinuity and the remote region which is assumed to be continuous in micro-scale. In fact, the process of fracture growth is described by the transition of the material behavior in the FPZ from micro-scale continuum to micro-scale discontinuum due to initiation and propagation of micro-cracks. These micro-cracks inside the FPZ then coalesce to form a macro-scale discontinuity represented as fracture surfaces. In other words, the FPZ acts as a bridging zone between cracked region and uncracked region. This transition process dissipates strain energy to create new micro-cracks and damage zones. Therefore, more efficient energy dissipation mechanisms in the FPZ, and bigger sizes of process zone lead to higher energy dissipation which can be regarded as higher resistance of the materials against failure and fracturing. This is the reason why the fracture energy is significantly influenced by the FPZ characteristics. The stages of the development of the micro-crack damage zone around a crack tip in rock have been described in Hoagland et al. [5].

There have been mainly two models to estimate the size of plastic zone under mode I loading: The Irwin approach, and the strip-yield model. Irwin [39] estimated the plastic zone size by equating the normal stress along crack plane to the yield stress. This first approximation was then improved by considering the stress redistribution along the crack plane, giving a simple formula of $L_I^p = (K_I/\sigma_u)^2/\pi$, where L_I^p is the size of plastic zone in the crack plane, K_I is the mode I stress intensity factor and σ_u is the yield strength. The strip-yield model was proposed independently by Barenblatt [40] and Dugdale [41], and considers the inelastic zone in front of the crack tip as a part of a larger crack extending to the end of inelastic zone and having a uniform cohesion stress equal to a yield strength applied on its boundary. The method uses superposition principle to give an approximation of inelastic zone which vanishes the stress singularity, and gives a simple approximation of $L_S^p = \pi(K_I/\sigma_u)^2/8$. Irwin and strip-yield models predicts close values for the size of the plastic zone for small values of K_I/σ_u . For brittle material, one can simply replace the yield strength σ_u by the tensile strength σ_t to estimate the size of the FPZ. The size of a fully developed FPZ on the onset of fracture propagation ($K_I = K_{Ic}$) is given by $L_I = (K_{Ic}/\sigma_t)^2/\pi$ and $L_{Su} = \pi(K_{Ic}/\sigma_t)^2/8$ based on Irwin and strip-yield models. These estimations assume a uniform stress being applied along the length of the FPZ, and therefore they are not expected to give very accurate predictions of FPZ length since the inelastic deformation has the nature of micro-damaging rather than plasticity in quasi-brittle materials. Taking into account a linear reduction of traction with proximity to the tip, Labuz et al. [42] modified the strip-yield model to adjust for the micro-damaging of the rock material in the FPZ. This approximation gives a longer FPZ length with the relation $L_{S_l} = 9\pi(K_{Ic}/\sigma_t)^2/32$. Since both K_{Ic} and σ_t are considered material properties, the size of the FPZ is also expected to be a material property.

Models describing the shape of the inelastic zone are based on determining the boundary of a region within which a component or invariant of elastic stress exceeds the yield stress. Unlike the metals in which a distortion-based criterion like Von Mises governs best the plastic behaviour, the nonlinear micro-crack zone in quasi-brittle materials is mainly developed due to the tensile stress. The most well-known criterion to describe the shape and size of the FPZ is the maximum normal stress introduced by Schmidt [43]. According to this criterion, the FPZ is formed in the region where the local maximum principal stress exceeds the tensile strength of the material. This model uses the elastic stress field near the tip and solves for the boundary of the region where maximum principal stress reaches the strength. This model, however, does not account for the redistribution of stress outside the FPZ while inelastic deformation occurs inside the FPZ, and therefore underestimate the size of the FPZ. As will be explained later, most of the experiments suggest a band-shaped (semi-elliptical) process zone for quasi-brittle materials which does not match the butterfly shape suggested by Schmidt [43]. The main reason might be that the Young's modulus reduces mainly in the direction normal to the fracture plane in the process zone, and the reduction of strength within the process zone due to micro-cracking may lead to elongation of the process zone. One therefore should account for the reduction of elastic properties and strength, perhaps using an anisotropic damage model, in order to provide a better model for the shape of the FPZ in quasi-brittle materials.

The FPZ size and shape are expected to depend only on the loading mode of the crack and the material properties and not on the specimen configuration. However, this is only true when the material properties such as K_{Ic} and σ_t do not exhibit specimen size and configuration dependence. For example, K_{Ic} is dependent on the size of specimen for smaller specimens mainly for two reasons: (i) the LEFM theory is unable to give good approximation of stress field when the FPZ is large compared to the crack size, (ii) even if one still considers the LEFM theory for crack with large nonlinear zones, the FPZ is likely to develop outside the singular dominant region, where only singular terms of the crack elastic solution are not sufficient to characterise the stress field. In other words, when the FPZ is large enough compared to the size of the crack and crack ligaments, higher order terms of the elastic solution also play a role in stress characterisation near the crack tip, and influence the FPZ development [44,45]. This is why the FPZ is also specimen size dependent for small specimens. Experimental observations also indicate that the boundary of specimen can influence the size of the FPZ and prevent the FPZ to develop fully [46]. The significant size of the FPZ compared to the specimen size is the main reason for the size dependency of strength and fracture toughness. This is why the FPZ plays an important role in determining a characteristic length of the micro-structure that reflects size effects. The fracture energy is closely related to the FPZ size and this implies that the existence of a FPZ may be the intrinsic cause for size effects. The applicability of linear elastic fracture mechanics for analyzing cracked

structures is therefore determined by how big the FPZ is compared to the size of the specimen.

3.2. Experimental methods to evaluate FPZ

The importance of the FPZ in understanding the size effect phenomenon in quasi-brittle materials has encouraged many researchers to experimentally observe the development of the FPZ. The observation of fracture process zone is difficult because of the small scale at which micro-structural events occur. The experimental techniques used to determine the FPZ in quasi-brittle materials can be divided into three categories:

- **Visual and image-based** methods such as optical and photoelectron microscopy, moiré interferometry, and digital image correlation (DIC): These methods rely on the analysis of images obtained from the surfaces of cracked specimens. The region of inelastic deformation is then identified by analyzing the changes in the surfaces due to highly localized strain near the tip of fractures [47,48]. DIC has been particularly popular recently due to simplicity, availability and the fact that it can provide a very accurate full-field measurement of strain field [49–51]. The resolution of the full-field data obtained from the DIC is considerably high, often below 1 μm .
- **Acoustic-based** methods such as acoustic emission and ultrasonic probing: These methods utilize the information obtained from active and passive seismic waves traveling within the cracked specimens. Acoustic emission analyses the micro-seismic events generated by the inelastic mechanisms like micro-cracking and traces the location of micro-seismic event [46,52,53]. Ultrasonic probing, on the other hand, analyses the attenuation of active ultrasonic waves when they travel through a region of high inelastic deformation [54–56].
- **Mechanical property-based** methods such as microhardness and nanoindentation: These methods are based on using nano- or micro-indentors to perform small scale load tests around the tip of cracks. A change in hardness is expected inside the FPZ since the material has undergone inelastic deformation. The boundary of the FPZ can then simply identified based on the change in hardness. Plastic deformation in metals is often accompanied with an increase in nanomechanical properties whereas damaged zones in quasi-brittle materials have a reduction in nanomechanical properties [57–59].

A noteworthy review of the works done using most of these techniques is given in Brooks et al. [58]. Among methods mentioned above, the AE and DIC seem to have attracted a lot of attention. The ability of AE to trace the inelastic deformation not only on the surface but also inside the cracked specimens has made this method very powerful for characterising the FPZ. The main drawback of this method is high possible errors in determining the events' locations due to the uncertainty in the velocity model. Alam et al. [60,61] used both the AE and DIC simultaneously and concluded that material damaging can change the velocity model significantly, and the location inaccuracy in their experiments is in the range of 5 mm. Therefore, an accurate determination of the FPZ size can be difficult to achieve with the AE. The DIC, on the other hand, provides very accurate full-field displacement and strain measurement on the surfaces of the cracked specimens. When performed using high-speed camera, the DIC is able to trace the mechanisms of fracture growth at the peak load very accurately.

3.3. Lessons learned from past experiments

On the basis of the results obtained from different experimental techniques used to characterise the FPZ in quasi-brittle materials, we can summarize the current knowledge as following:

1. There is a general consensus among the researchers that a positive correlation exists between the grain size (aggregate size in concrete) and the width of the FPZ. This means that the larger the grain size, the bigger the FPZ width in quasi-brittle materials [47,57,59,62,63]. Zietlow and Labuz [46] measured the width of the FPZ for four different rock types and suggested that there exists a linear relation between the FPZ width and the logarithm of the grain size. The reason for this trend is perhaps due to a relation between the grain size and micro-crack density. Finer grained materials develop more micro-cracks in their damage zones than coarse-grained materials. In other words, the finer-grained materials dissipate energy more efficiently with respect to space, and therefore can develop a smaller damage zone before fracture [59].
2. There seems to be an inverse correlation between the grain size and fracture toughness/tensile strength. Finer grain materials dissipate energy more efficiently in their smaller FPZ than coarse-grained materials in their larger FPZ, and thus attain higher strength properties [59,64]. The experiments also show that as the grain size decreases, micro-crack density increases, which means that finer-grained materials have more micro-cracks in their damage zones than coarse grained materials [59]. However, this is a strong statement and needs more supporting evidence.
3. Results from different experiments agree that the micro-crack density increases exponentially within the FPZ by approaching the fracture or fault [52,65–69]. Microhardness and nanoindentation experiments also confirm that the regions of increased micro-cracking aligns with regions of reduced nanomechanical properties [58]. This indicates the reduction of mechanical properties is due to the micro-cracking [59]. Micro-cracks were also found to be mainly orientated parallel to the fracture [68].
4. Many experimental data show that the process zone is of a semi-elliptical (narrow-band) shape [46,47,49,52,54,62,70]. This structure conforms well with the assumption of cohesion-based process zone along the crack plane in the strip-yield (Dugdale-Barenblatt) model. In fact, it has been shown that the narrow-band shape of the FPZ is in a good agreement with the Dugdale-Barenblatt model [47,65,66,68]. Micro-structure analyses by Nasserri et al. [68] also show that micro-cracks in the FPZ are mainly

oriented parallel to the fracture, which justify the formation of a band-shaped FPZ. From the results on sandstone, Backers et al. [52] also observed a semi-elliptical FPZ with a length and width of about 20 mm and 10 mm. The width of the FPZ is often regarded as the characteristic length of micro-structure, and has been introduced into non-local and strain-gradient damage models to describe the width of localized zones. This often leads to capturing a deterministic size effect of quasi-brittle materials. The length seems to depend on the rate and the significance of material softening. The arising question is in fact if there is any relation between the width and the length of the FPZ.

5. The FPZ size seems to be dependent on the specimen size for smaller samples. This is due to the proximity of specimen boundary to the crack tip. Experimental data on concrete suggests an increase of the FPZ length with the increase of the sample size [49,62]. In fact, the main sample size parameter influencing the FPZ length is the ligament size, which is the distance between the crack tip and the closest boundary. The trend shows that the FPZ length becomes smaller as the ligament size decreases. This is due to the boundary constraint in front of the crack tip, that does not allow the FPZ to fully develop. Despite the strong dependency of length on size, the width seems to hardly show any dependency on the specimen size [62,70,71].
6. Near the peak load, the length of the FPZ exhibits more load-dependency than its width. Experimental results from both AE and DIC show that the FPZ width almost stabilizes at about 70–80% of the pre-peak load whereas its length exhibit a significant load-dependency starting at 80% of pre-peak and continuing over the post-peak period [60,63,72]. This indicates that the formation of macro-cracks (micro-crack coalescence) which occurs near the peak-load does not significantly influence the width of the FPZ while it has a strong influence on the length (see results of Wu et al. [49]). The increase of load generally causes the activation of more micro-cracks. However, it seems that near the peak load, the main energy dissipation mechanism is the coalescence of previously activated micro-cracks. Since the micro-cracks are oriented in the direction of the main crack as mentioned previously, the width is not influenced by micro-crack coalescence, while the length significantly depends on that because damage and degradation continues extending the FPZ in the direction of main crack.
7. The FPZ size identified by AE is much larger than the one obtained by microscopy [56,62,67,52]. This may be because there is generally a high uncertainty in locating acoustic emissions due to uncertainty in the velocity model resulted from rock anisotropy and heterogeneity. Another reason for this behaviour may be the fact that the AE is able to locate all the local failures within the body while the microscopic analyses are only surface measurements.
8. Results from AE measurements show that both tensile and shearing events are captured even when the macro-crack is subjected to pure mode I [52,61,68]. This can be explained by taking into account the fact that in essence micro-cracks are randomly oriented, and some are more susceptible to shear than tensile failure, and therefore one should not expect only tensile failure in mode I loading of original main crack. In addition, under mode I loading, the shear stress is zero only along the crack ligament, and significant shear stresses are present at other directions. These results generally suggest that both tensile and shearing failures occur in the micro-scale irrespective of the type of the loading applied on the original macro-crack.
9. Experiments on the FPZ characterization under mixed-mode loading condition show that the FPZ slightly rotate from the crack plane, and both crack opening and sliding occur at the crack mouth [51,73].

3.4. FPZ evaluation using DIC

DIC is a relatively new method in experimental mechanics, whose popularity was favored by the advancements in imaging and digital image processing techniques. The DIC uses consecutive imaging of the surface of a deforming body, whose surface is covered in a random speckle pattern, and calculates the surface position and displacements by correlating the patterns in space and time. Through high resolution and high speed cameras, and through the availability of robust numerical algorithms for cross correlation, the DIC is nowadays a powerful technique in experimental mechanics, and is able to provide high resolution and precise measurements of surface displacements and strains. For this reason, DIC has been widely used recently for investigating the inception and the evolution of the strain localization in quasi-brittle materials. However, when using DIC for evaluating localized deformation in the FPZ, the calculated displacements and strains can be sensitive to length resolution, search patch size of images and filter size used for smoothing purposes.

The following methods have been used to determine the FPZ from DIC:

- The most simple method is based on the jump of displacement across the crack plane [49–51,71,73,74]. Based on this scheme, the distance between the two ends of the displacement jump at either sides of crack plane denotes the FPZ width, while the distance from the tip up to the point along the crack ligament at which displacement jump vanishes denotes the FPZ length. It is noteworthy that the evolution of the displacement jump by load shows three different stages: (1) Elastic phase in which no considerable jump is recognizable, (2) formation of the FPZ with moderate displacement gradient, and (3) very high gradient of displacement which occurs at the moment of instability and macro-crack initiation. The width of the FPZ shall be measured towards the end of the second phase which is expected to be near the peak load on the force-displacement curve. At any stage after this point, the opening of macro-crack surfaces known as the crack tip opening displacement has to be deduced from the distance between the two ends of the displacement jump in order to obtain a valid FPZ width. The crack mouth opening and its variation along the FPZ can also be evaluated using this method. Most of studies show a somewhat linear reduction of opening along the FPZ.
- The second method is based on strain contours and using a critical strain as a threshold to define the FPZ [60,70,75]. Although strains are good indicators of localised zones, one needs to address the following issues when using this method: (1) How the accuracy of calculated strains in the FPZ is influenced by subset size, subset distance and filter size. (2) What value is suitable for

the critical strain and which component or invariant of strain tensor shall be used.

- Skarzyński et al. [72] and Skarzyński and Tejchman [63] discussed the objectivity of the DIC measurements at localized zones, and suggested a third method. It uses the error function to fit the displacement jump, and the normal distribution function to fit the strain variation along a path crossing the crack plane. Their results show that the FPZ size obtained from the displacement is different from the one obtained from the strain. The average of the fitting parameters for the displacement and strain with different search patch sizes is suggested to be used to define the width of the FPZ. Their suggested method also calculates different values for the size of the FPZ when using different software.

4. Experimental setup

4.1. The rock samples

In order to conduct the fracture toughness and strength tests, all samples were obtained from the cores extracted from the Grimsel Test Site (GTS) in the central Swiss Alps, Switzerland, which is part of the Aare massif. The rocks found in the rock laboratory consists of granitic to granodioritic composition. The material originates from the borehole FBS16.003, which was drilled during the In-situ Stimulation and Circulation (ISC) experiment in this rock laboratory [1,76]. The borehole has a length of 44 m, a diameter of 87 mm, azimuth of 219.9° and dip of 37.3°. The foliation (175/75°) in the axial plane of the core dips with approximate 11°, which makes the foliation plane almost parallel to the axis of the cores. The specimens are cut from the borehole interval 38 to 39 m for Brazilian tensile tests and 43 to 44 m for the fracture toughness tests. All the specimens were dried for 24 h at 105 °C three days before testing.

The lithology of the tested material consists of the so-called Grimsel Granodiorite which has a magmatic fabric, which is coarse-grained, massive and slightly porphyritic [77–79]. The rock is mainly composed of phyllosilicates, feldspar and quartz, with the volumetric ratios of 28% kalifeldspar and 36% plagioclase and 36% quartz, which is close to the mineralogical transition between granodioritic and granitic composition. The quartz occurs in mm sized grains, while the orthoclase shows a few mm sized grains with Carlsbad-Twins and the plagioclase occurs from a few 10 microns to mm sized grains. Biotite occurs as predominant phyllosilicate and defines a strong foliation. During Alpine orogeny, strong textural overprinting of the rock occurred. The maximum pressure and temperature conditions are of greenschist conditions with 450 ± 30 °C and around 6 ± 1 kbar pressure [80]. The plagioclase is saussuritised and mainly persists as albite and epidote. The biotite is partly displaced by chlorite during hydrothermal fluid circulation. The planar minerals are adjusted to the Alpine foliation, such that the naming by geological terminology is a Gneiss. The presence of aligned phyllosilicates implies that grain boundaries are preferentially aligned with the schistosity. The grain boundaries are initiation points for the micro-fracturing process. In the reminder of the paper, we will associate them with pre-existing micro-cracks and refer to them simply as micro-cracks.

A specific model of anisotropic elasticity is the transversely isotropic constitutive law, which is suitable for predicting the deformational behaviour of many types of rocks including the Grimsel Granodiorite. The transversely isotropic model defines a so-called isotropy plane, which is assumed to coincide with the apparent foliation plane, and postulates that every plane transverse to it also defines a symmetry plane. Dambly et al. [81] investigated the orientation of the isotropy plane in Grimsel Granodiorite and concluded that the isotropy plane coincides with the foliation plane with a good accuracy. Hereafter, the foliation plane is used to refer to the isotropy plane in a transversely isotropic model. Five elastic constants characterize the elasticity of the transversely isotropic material in principal coordinates: Two Young's moduli, E and E' , are defined within and normal to the isotropy plane, respectively; two ratios, ν and ν' , represent the Poisson's ratios within and normal to the isotropy plane, respectively; and a transverse shear modulus, G' , which defines the shear modulus in the direction transverse to the isotropy plane. Through the well-known Saint-Venant relation, an approximation for G'_{sv} can be obtained through the other elastic constants: $1/G'_{sv} = 1/E + 1/E' + 2\nu'/E'$. In reality, G' is an independent constant and can deviate from the approximated G'_{sv} . The in-plane shear modulus, G , is dependent of E and ν and is given by the relation $G = E/[2(1 + \nu)]$. Table 2 lists the five elastic constants averaged from different tests and measured for the Grimsel Granodiorite samples [81,82].

4.2. Fracture toughness and strength measurement

Fig. 1 shows schematically the geometrical configuration of the Brazilian and SCB samples used for tensile strength and fracture toughness measurements. The isotropy plane makes angle φ with the load axis in both SCB and BD tests. The geometrical details of the samples are given in Table 3. The fracture toughness tests were conducted using four configurations $\varphi = 0^\circ, 45^\circ, 60^\circ, 90^\circ$, while only two configurations of $\varphi = 0^\circ, 90^\circ$ were tested for tensile strength measurements.

The prepared samples for fracture toughness were tested in a Zwick/Roell Z005 AllroundLine uniaxial press with maximum applicable force of 5 kN and linear variable displacement transducer (LVDT). A three-point-bending fixture with central loading stamp of 10 mm diameter was employed. To start the test, the specimen was preloaded with 1 N. Thereafter, the Zwick universal

Table 2

The five elastic constants measured for Grimsel Granodiorite from uniaxial compression tests.

E	E'	G'	ν	ν'
42 GPa	21 GPa	17 GPa	0.2	0.1

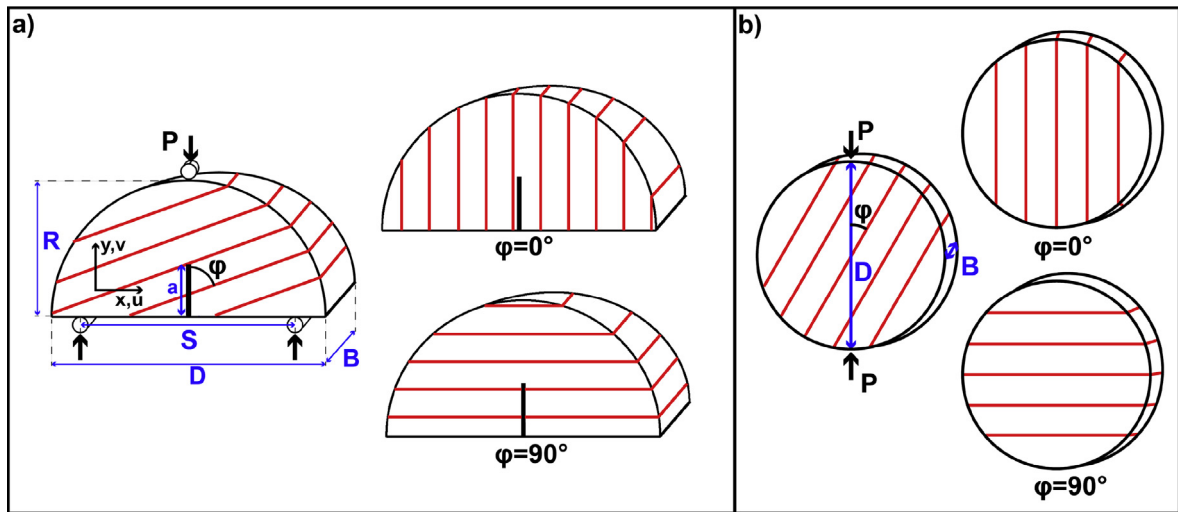


Fig. 1. Schematics of (a) Semi-circular bending and (b) Brazilian disk specimens, with their two end members $\varphi = 0^\circ, 90^\circ$ where φ is the angle between isotropy plane and the loading direction. A picture of the Brazilian disk with the apparent direction of isotropy plane (foliation) is also shown.

Table 3

Geometrical dimensions of specimens used for semi-circular bending (SCB) and Brazilian tensile (BD) tests.

Parameter	SCB		BD
	Values [mm]	Dimensionless values	Values [mm]
Diameter (D)	82.9		83.3
Thickness (B)	37–39	$B/D \approx 0.46$	37.3–40.3
Radius (R)	39.4–41.7		
Span length (S)	58.4	$S/D = 0.7$	
Crack length (a)	17–20	$\alpha = a/R = 0.41–0.5$	

testing machine was driven by a displacement criterion of 0.1 mm/min. After the load drop of 80% due to breaking, the Zwick universal testing machine stops the loading.

The Brazilian tensile strength specimens were tested in a Zwick/Roell 1474 RetroLine universal testing machine capable of reaching a maximum force of 100 kN. A curved loading jaw was used to distribute the load over a portion of disk’s circumference and avoid point load. To start the test, the specimen was preloaded with 5 N. Thereafter, the Zwick universal testing machine was driven by a displacement criterion of 0.05 mm/min. For both SCB and Brazilian disk tests, the load and the LVDT displacement were recorded by the digital acquisition system 1 (DAS 1). Both machines have a load resolution of 10 N and data were acquired with a rate of 100 Hz.

4.3. Digital image correlation

One side of the samples were coloured white and then were sparkled by an air brush to generate a random speckle pattern. We used a VIC-3D Digital Image Correlation System, which consists of two Prosilica GT 3400 9.2 Megapixel B/W cameras, with 80 mm focal length and capturing images with a sampling rate of 4 fps. The cameras were connected to the second digital acquisition system 2 (DAS 2). The two acquisition systems were synchronized by acquiring the force signal from the load cell with both the universal testing machine and the ADC converter of the DIC equipment. A reference image was recorded before deformation and a series of images was recorded during the tests. The resolution of this method depends directly on the speckle pattern on the specimen. Well-distributed and fine speckles allow to decrease bias and noise.

The DIC system was calibrated using a reference target reaching a calibration score (as defined in the software VIC-3D 7) of 0.018 pixels. The system setup, with the aforementioned choice of lenses, results in an average resolution of 40 pixels per millimeter. The subset size for the correlation process was chosen as a square with edge size of 35–47 pixels with a step size of one third of the edge size between subset centers, to deliver an average uncertainty throughout the area of interest of 0.01 pixels. This assumption was verified in the post-processing phase, and the average uncertainty for a representative test of 0.01 pixel was obtained. The DIC-system was started at the same time as the Zwick universal testing machine and stopped after total failure.

The series of images for each test were post-processed with VIC-3D 7 software [83]. The squared subset was correlated using Gaussian weight with an optimized 8-tap interpolation and normalized squared difference criterion. For consistency threshold,

confidence margin and maximum margin was set to 0.05 pixels in the VIC-3D software. The strain calculation in VIC-3D depends on the step size and on the filter size. Smaller step sizes increase the calculation time, which is accepted. A sensitivity analysis was performed to investigate the effect of the FPZ width varying resolution edge size, search patch size and filter size at different pre-peak load. The FPZ width was compared from the u -displacement jump and the width of the ϵ_{xx} -strain field. It was found that keeping the step size at one third of the subset size and having a filter size between 5 and 9 points can reliably identify the FPZ (details given in Section 6.1). Since noise level increases at such small filter sizes, an averaging scheme was used to reduce the effect of noise. MATLAB [84] was used for subsequent visualisation and further calculations.

5. Experimental results on toughness and strength

5.1. Fracture toughness anisotropy

Table 4 presents the geometrical details, the failure load as well as the calculated values of fracture toughness for 23 samples tested at different directions with respect to foliation (φ). Fig. 2a illustrates these data with respect to the normalized crack length, and Fig. 2b shows the variation of normalized fracture toughness values against the angle φ . The normalization is performed with respect to the mean value of fracture toughness at the configuration $\varphi = 90^\circ$ which corresponds to $1.66 \text{ MPa}\sqrt{\text{m}}$. The mean values are shown by black asterisks in Fig. 2b.

The mode I fracture toughness is calculated based on the normalized stress intensity factor Y_I and the maximum load P_m as [11]

$$K_{Ic} = Y_I \frac{P_m \sqrt{\pi a}}{DB} \quad (1)$$

where

$$Y_I = -1.297 + 9.516 \frac{S}{D} - \left(0.47 + 16.457 \frac{S}{D}\right) \alpha + \left(1.071 + 34.401 \frac{S}{D}\right) \alpha^2 \quad (2)$$

Here, a is the crack length, and B and D are the specimen thickness and diameter. The normalized stress intensity factor Y_I is a geometrical factor obtained from a fit to finite element (FE) results, and is valid only for isotropic materials [11]. In anisotropic cases, in addition to geometrical configuration, the material constants also influence the stress intensity factor solution. Several finite element analyses were performed to evaluate how strongly an anisotropic material model influences the stress intensity factor solution Y_I . The specimen was modeled and analyzed with the commercial finite element code ABAQUS. The finite element mesh and boundary condition are shown in Fig. 3. An anisotropic elasticity model was used to define the transversely isotropic properties given in Table 2. The contour integral module of ABAQUS uses cylindrical domains to calculate the interaction integrals and subsequently the stress intensity factors [85]. The domain integral method to calculate the stress intensity factors has been successfully used for isotropic materials [86,87], as well as anisotropic elasticity models [88–90]. Upon the calculation of the stress intensity factors, the normalized stress intensity factors Y_I and Y_{II} are obtained from

Table 4

Values of the fracture toughness measured for different angles between foliation and initial crack (φ).

φ	Sample ID	α	B [mm]	Y_I	P_m [N]	K_{Ic} [MPa $\sqrt{\text{m}}$]	Average K_{Ic}
0°	FT01	0.506	39.4	5.79	1410	0.65	0.73 ± 0.09
	FT02	0.487	39.3	5.53	1810	0.77	
	FT05	0.417	39.1	4.78	2550	0.88	
	FT06	0.429	38.3	4.88	2200	0.82	
	FT15	0.495	39.2	5.64	1410	0.63	
	FT16	0.503	39.4	5.74	1420	0.65	
	FT21	0.412	37.3	4.73	2040	0.72	
45°	FT11	0.421	36.9	4.81	2760	1.03	0.99 ± 0.06
	FT12	0.415	36.7	4.76	2520	0.92	
	FT13	0.501	38.5	5.72	2100	0.97	
	FT17	0.429	37.3	4.89	2360	0.90	
	FT18	0.428	36.9	4.88	2830	1.08	
	FT25	0.514	38.1	5.89	2070	1.01	
60°	FT27	0.514	37.5	5.89	2410	1.21	1.30 ± 0.10
	FT28	0.484	37.6	5.50	3170	1.40	
90°	FT03	0.491	38.3	5.59	4010	1.80	1.66 ± 0.15
	FT04	0.495	38.3	5.64	3360	1.54	
	FT08	0.484	39.1	5.50	3510	1.50	
	FT09	0.491	36.3	5.59	4000	1.89	
	FT19	0.456	37.8	5.17	3540	1.47	
	FT20	0.427	37.6	4.87	4810	1.79	
	FT23	0.481	38.5	5.46	4020	1.72	
	FT24	0.514	38.1	5.89	3180	1.58	

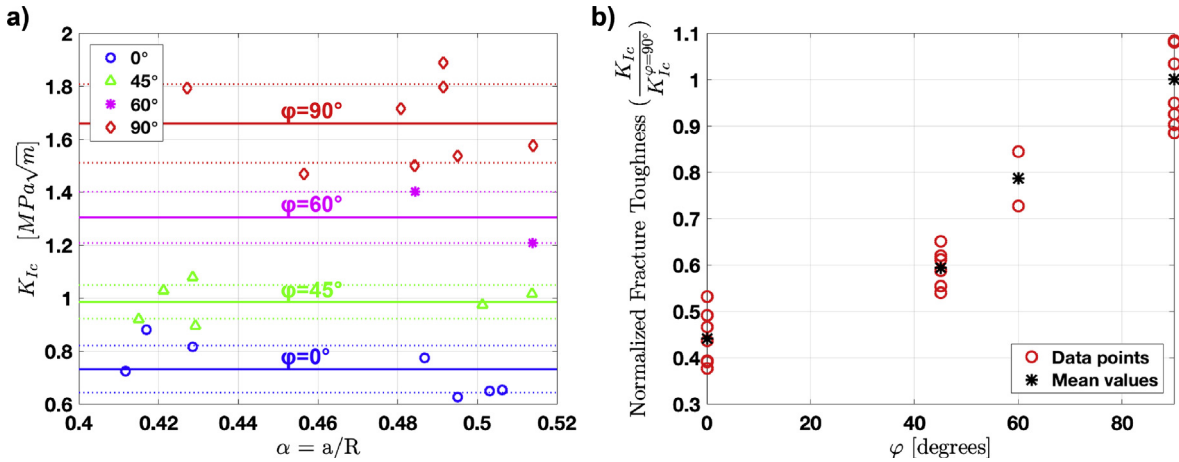


Fig. 2. (a) The variation of fracture toughness against the dimensionless notch ratio α for different angles between the foliation and the crack orientation. The solid and dotted lines indicate mean and standard deviation (SD), respectively. (b) The variation of normalized fracture toughness to the mean value at $\varphi = 90^\circ$ against the angle between foliation and direction of initial crack φ .

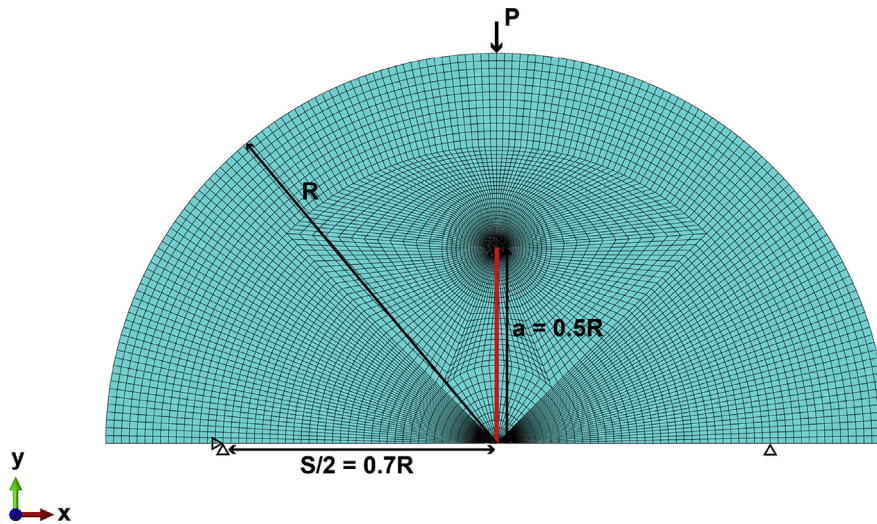


Fig. 3. The finite element mesh and the boundary condition used for the finite element analyses of the SCB specimen.

$$Y_I = \frac{K_I BD}{P\sqrt{\pi a}}, \quad Y_{II} = \frac{K_{II} BD}{P\sqrt{\pi a}} \tag{3}$$

using the geometrical and loading values employed in the finite element model. The finite element results for isotropic as well as anisotropic material models are compared in Table 5. The values obtained from Eq. (2) are also given for comparison. It is seen that the influence of anisotropy on the values of the normalized stress intensity factors is minimal.

The results indicate the following: (1) Y_I obtained from the formula given in Kuruppu et al. [11] overestimate the fracture toughness by only 2%. (2) The influence of the anisotropy on the stress intensity solution Y_I is negligible. (3) Although the cases $\varphi = 0^\circ, 90^\circ$ still induce pure mode I using an anisotropic elasticity model, the configurations $\varphi = 45^\circ$ yield a mixed-mode I/II type with $K_{II}/K_I \approx 0.1$. This indicates that the results obtained for $\varphi = 45^\circ, 60^\circ$ are not in fact pure mode I fracture toughness. Note that the

Table 5
Comparison of normalized stress intensity factors obtained from isotropic and anisotropic solutions.

φ	Y_I			Y_{II}
	Eq. (2)	Isotropic (FE)	Anisotropic (FE)	Anisotropic (FE)
0°	5.657	5.557	5.619	0
45°			5.658	-0.640
90°			5.527	0

influence of the anisotropy on the stress intensity factor solution can be more significant in other samples, configurations and anisotropy ratios.

Analyzing the fracture toughness results, the following remarks are noted:

- The values of fracture toughness are not influenced by the dimensionless notch length. It is known that for small samples, the fracture toughness can be significantly influenced by the ligament size. These results therefore seem to imply that the samples are large enough to be suitable for fracture toughness measurement of the type of rock under study.
- The ratio of the maximum fracture toughness to its minimum is 2.27, which indicates a strong anisotropy in fracture toughness. The fracture toughness is the largest for crack propagating normal to the foliation, and is the minimum when the crack grows along the foliation.
- Although the configurations $\varphi = 0^\circ$ and $\varphi = 90^\circ$ correspond to pure mode I crack deformation, the configurations $\varphi = 45^\circ$ and $\varphi = 60^\circ$ involve mixed mode I/II crack growth. This is due to the elasticity anisotropy.
- Normalizing the values of the standard deviation with respect to the actual values of the fracture toughness gives $0.73 \pm 12\%$, $0.99 \pm 6\%$ and $1.66 \pm 9\%$ for $\phi = 0^\circ$, 45° , 90° , respectively. The comparison of the standard deviations shows no significant variation of the scatter from one configuration to another. The reason for this small difference in scatter can be attributed to the heterogeneity and large grain size of the rock under study. Any conclusion on the difference of the scatter of the results between different configurations requires a bigger data set where the effect of heterogeneity between different configurations is minimized.

5.2. Post-mortem fracture surface analyses

Post-mortem analyses of fracture surfaces help to understand the fracturing processes in different configurations. Such analyses may also be used to validate the accuracy of test conditions for mode I fracture toughness measurement as explained by Kuruppu

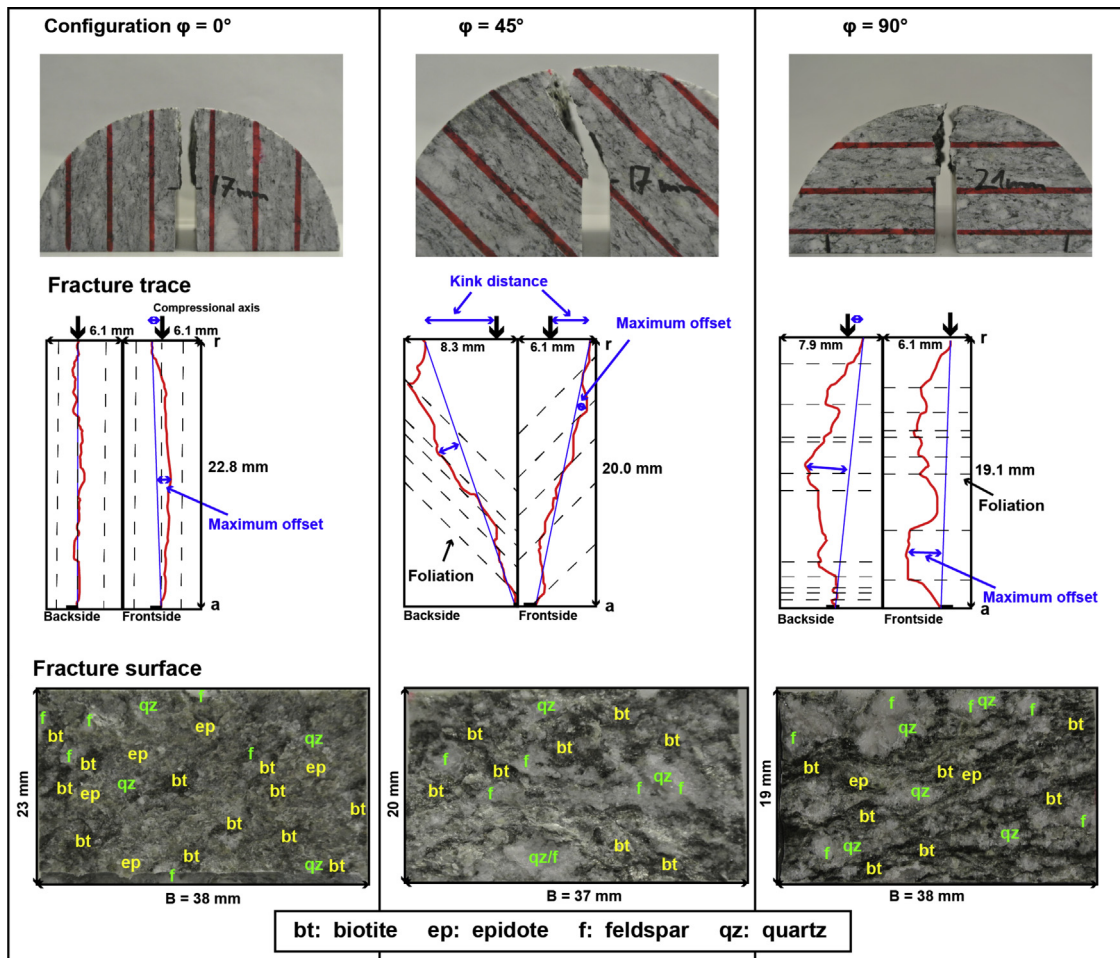


Fig. 4. The visual analyses of fracture traces and surfaces for three angles between initial crack and foliation: $\varphi = 0^\circ$, 45° , 90° .

et al. [11]. According to these guidelines, a deviation of more than $0.05D$ (equivalent to 4.1 mm in our samples) of the cracked ligament from the notch plane makes the test invalid, with the resulting value being not representative of mode I fracture toughness. Fig. 4 illustrates the fracture trace, both front and back views, together with the mineral analyses of fracture surfaces of all different configurations. The fracture trace is described in terms of two length parameters: maximum offset indicates the maximum distance between the fracture path and the line connecting the start and end points of the generated fracture; and kink distance is the distance between the end point of generated fracture from the loading point. The type of the minerals in the new fracture surface are also analyzed macroscopically.

In the case of fracture growth along foliation ($\varphi = 0^\circ$), the fracture path shows very small values of kink distance (about 1 mm) and maximum offset (about 2 mm). The analysis of fracture surfaces show a high content of sheet silicates such as biotite and chlorite, indicating the fracture is aligned with the biotite-rich plane. Epidote, feldspar and quartz were also observed in the new fracture surfaces, with apparent average grain size of smaller than 4 mm. When the fracture growth is normal to foliation ($\varphi = 90^\circ$), the kink distance is still very low (about 2 mm), while the maximum offset (about 6 mm) is higher compared to results of $\varphi = 0^\circ$. The fracture seems to break through patches of stiffer quartz and feldspar rich layers, and this may be the reason why the fracture surfaces are rougher compared to the case $\varphi = 0^\circ$.

The fracture traces for $\varphi = 45^\circ$ show much higher kink distance, about 4–6 mm, compared to the other two configurations. These values are at the border or slightly higher than the limits set based on the guideline ($0.05D = 4.1$ mm), and therefore these test may not be considered as valid pure mode I fracture toughness tests. The maximum offset is about 4 mm which is more than $\varphi = 0^\circ$ and less than $\varphi = 90^\circ$. The highly kinked fracture path may indicate the presence of mode II loading, which is in agreement with what was noted in Section 5.1. However, one should also note that the crack kinking in anisotropic rocks can be present even for pure mode I loading condition since apart from the loading, the directional-dependency of the strength can also influence the fracture growth direction [91]. The fracture traces sometimes shortly align with the foliation plane and breaks sometimes through stiffer layers containing quartz or feldspar.

The following remarks are noted: (1) The fracture roughness is much higher in the case of $\varphi = 90^\circ$ compared to $\varphi = 0^\circ$, which seems to be the influence of aligned micro-cracks along the foliation. As the angle between foliation and the initial crack, φ , increases, the maximum offset also raises, which is consistent with rougher fracture surfaces. (2) The largest kink distance is observed in the cases of $\varphi = 45^\circ$, 60° . These cases show clear deviation from the original crack direction, which seems to be due to a mixed mode I/II crack loading. (3) As φ increases, the content of phyllosilicate minerals (e.g. biotite) on the fracture plane decreases. The fracture plane for $\varphi = 45^\circ$ shows a higher content of feldspar and quartz compared to the one from $\varphi = 0^\circ$ but less than $\varphi = 90^\circ$.

5.3. Strength anisotropy

This section presents the indirect tensile strength measurements using Brazilian disk tests. Table 6 lists the thickness, failure load and the calculated strength of six Brazilian disk specimens in two configurations $\varphi = 0^\circ$ and $\varphi = 90^\circ$. In order to calculate the strength, finite element analyses were performed to obtain the tensile stress at the center disk using the elastic constants of transversely isotropic elasticity model given in Table 2. It is evident that the strength is strongly anisotropic, with the value in the direction normal to the foliation being 2.61 times the one along the foliation. This indicates the principal role of micro-cracks dominantly aligned with the foliation on the strength of rock.

Many previous studies have employed the isotropic solution to calculate the strength from Brazilian disk. Table 7 presents the values of strength calculated based on an isotropic elasticity behavior in comparison with the ones obtained from the finite element solution of anisotropic model. It is clear that an isotropic assumption introduces a large error, 20% in the direction of foliation and 9% in the direction normal to foliation, in the calculation of strength. In addition, an anisotropy ratio of 2.01 is obtained from isotropic model, which is significantly lower than the anisotropic prediction. It is expected that the error stemming from the isotropic solution will increase with increasing elastic anisotropy.

The failure mechanism in two main directions also shows significant differences. The failure normal to the direction of foliation exhibits a more sudden and instantaneous behavior than the one along the foliation. In fact, the analyses of strains obtained from DIC measurement show the development of a band of failure along the foliation before the final rupture. This may indicate that the fracturing process is mainly due to the gradual activation of micro-cracks, which are mainly aligned with foliation, followed by their coalescence to form a macro-crack that splits the specimen. On the other hand, when the direction of final rupture is normal to the foliation, the existing micro-cracks cannot simply connect to form the fracture, and a more complex mechanism is required in the

Table 6

The tensile strength measurements using Brazilian disk tests. The tensile stress at the center of disk was obtained using finite element solution of a transversely isotropic model based on elastic constants reported in Table 2.

φ	B [mm]	P_m [kN]	σ_r [MPa]	Average σ_r [MPa]	Ratio
0°	39.5	32.39	5.50	5.63 ± 0.11	2.61
	38.6	34.3	5.68		
	40.3	36	5.71		
90°	38.9	74.2	16.07	14.69 ± 2.00	
	38.0	55.9	12.39		
	37.3	69.1	15.60		

Table 7

Comparison of average Brazilian disk tensile strength obtained from isotropic and transversely isotropic elasticity solutions.

φ	σ_t [MPa]	σ_t^{iso} [MPa]	$ \sigma_t - \sigma_t^{iso} /\sigma_t$ [%]
0°	5.63	6.73	20
90°	14.69	13.33	9

failure process perhaps including the development of new micro-cracks to connect the existing ones. Overall, the results emphasize the role of existing set of micro-cracks in the fracturing of granite, as it has also been observed in previous studies [64].

6. Experimental results on the FPZ

As discussed in the review given in Section 3, the characterization of the FPZ in quasi-brittle materials including rocks is of great importance, and is in fact a difficult task to conduct. Three suggested method to identify the FPZ from DIC results were also discussed. Due to the highly localized strain in the FPZ, the strain values should be used with caution when the FPZ is identified from strain results. Also, due to the small size of the FPZ, highly accurate DIC measurements are required. Therefore, an accurate determination of the FPZ requires highly accurate DIC results with appropriate smoothing methods to obtain strain in highly localized zones. This section introduces an averaging method to obtain reliable values for the size of the FPZ, and discusses anisotropy of the FPZ in anisotropic rocks. The calculated values are then compared to the values estimated by models based on linear elastic fracture mechanics.

6.1. Identification of the FPZ

The DIC method provides a full-field representation of in-plane surface displacements. The spatial gradient of the displacement field is then evaluated to obtain the strain field. Due to noises involved in the displacement measurements, smoothing techniques are used to obtain the derivatives. The subset size is defined as a squared window used to compare two different speckle-pattern and the step size is the spacing between the subset centers. In our case the measurement needs to cover a region of 8 cm × 6 cm and the recording resolution is 3384 pixels × 2704 pixels. The average accuracy allowed is set to 0.01 pixels. During the measurements, an average resolution of 40 pixels/mm was employed. The choice of the subset size between 35 and 41 pixels corresponds to 1 × 1 mm². The recommended step size is one-third of the subset size i.e. 13 pixels which is equivalent to 1/3 mm. This means that a 41 × 41 pixel area is tracked at every 13 pixels. The filter size is defined as the length of the displacement values at subset centers, which smooths the strain field with increasing number of displacement points. The strain field depends directly on the step size and the filter size of the strain tensor.

In this paper we use an averaging window to obtain the width of the FPZ, and compare this value with the one calculated from the jump in displacement. This averaging is required since small filters are insufficient to remove sufficient noise from the strain results.

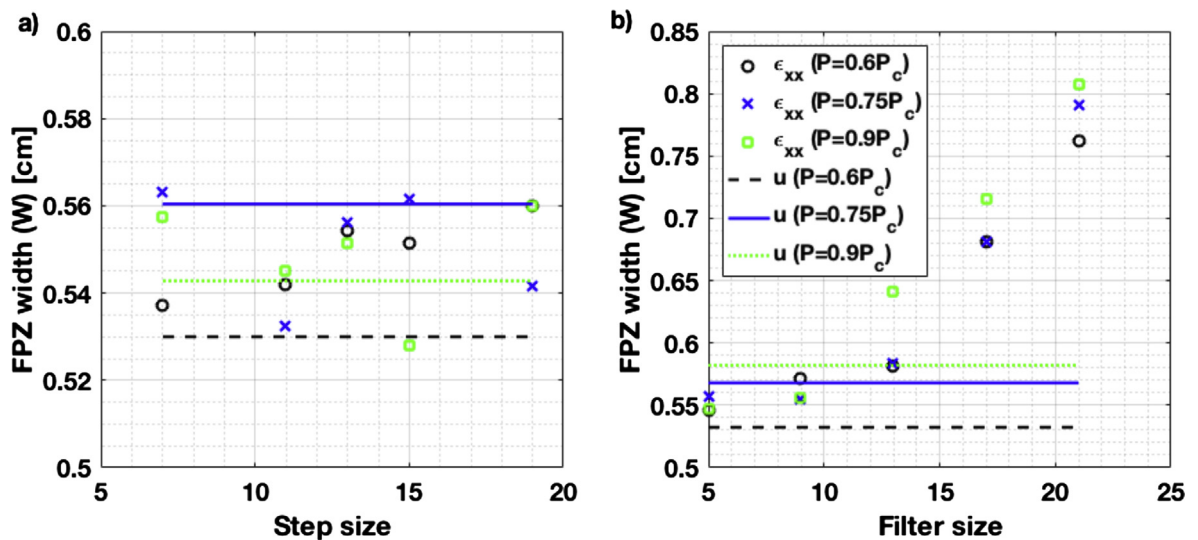


Fig. 5. (a) The variation of the FPZ width obtained from localised strain ϵ_{xx} and displacement jump u against (a) step size and (b) filter size, for three load levels of 60%, 75% and 90% of pre-peak load for a configuration $\varphi = 0^\circ$. The subset size for all measurements is thirty-nine pixels. In (a) and (b) the filter size and step size are five points, and thirteen pixels, respectively.

This methodology is based on a window containing ten paths with intervals of 0.5 mm crossing the crack ligament near the top. Averaging the strain and displacement then removes the local noises, and facilitate observing the localized zone even with very small filter sizes. There are mainly two parameters influencing the smoothing of strain measurements: step size and filter size. The shape and the length of the FPZ is also obtained using the variation of the maximum principal strain ϵ_1 along a path ahead of the crack tip. The length is evaluated based on the distance in which the maximum principal strain is highly localized. The shape can also be determined based on the values of the maximum principal strain.

Fig. 5 shows the variation of the FPZ width against the step and filter size at different load levels with respect to the peak (failure) load. The results in both Fig. 5a and b are obtained from the subset size of 39 pixels to deliver an average uncertainty of displacement resolution throughout the area of interest of 0.01 pixel. In Fig. 5a the filter size is kept constant at the minimum possible value (five points), while in Fig. 5b, the step size of thirteen pixels is used. The displacement values are not influenced by the step size and filter size since these parameters are only involved in the post-processing stage to obtain strains from displacements. These two plots suggest two main trends:

- As long as the filter size is chosen to be a small value, the calculated value for the width of localized zone is not influenced by the value of step size, and the width obtained from strains and displacement are in very good agreement. This suggest that given an appropriate choice of filter size, the step size recommended by the software (one-third of the subset size, thirteen pixels in our case) can be reliably used.
- At the constant step size, as the filter size approaches its minimum (five points), the width obtained from strain approaches the one obtained from displacement. Moreover, the calculated width from strain increases linearly for filter sizes above ten points. This suggests that high values of filter size increases the size of the region in which a strain smoothing procedure is applied, and therefore if the smoothing region is greater than the half of the FPZ width, the sharp displacement jump at the middle of the FPZ widens the strain profile, which leads to inaccurate measurement of the FPZ width from the strains.

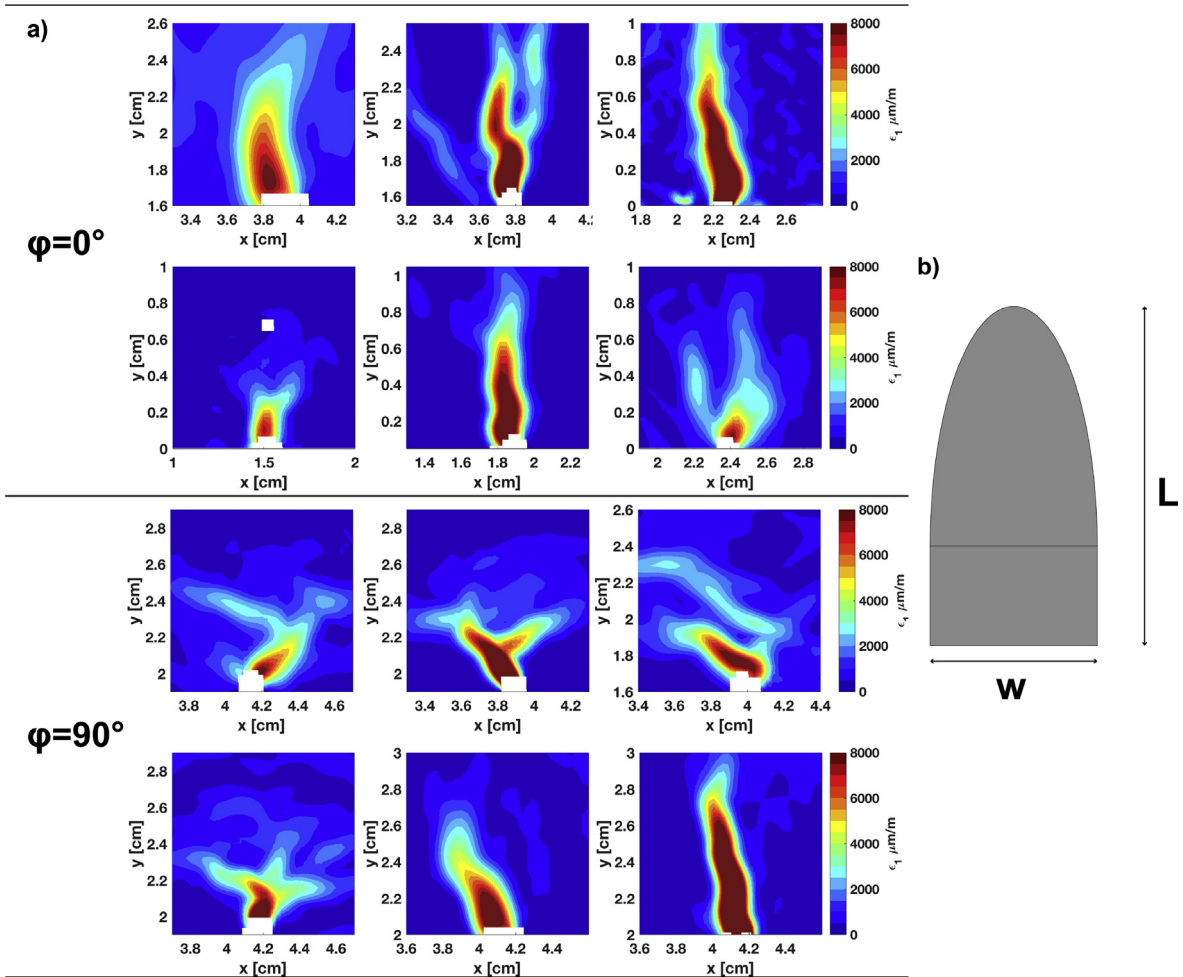


Fig. 6. (a) The contours of maximum principal strain showing the FPZ shape at peak load for the configurations $\varphi = 0^\circ, 90^\circ$. (b) The FPZ is idealized schematically as a semi-elliptical region with the width of W and the length of L .

An example to clarify the influence of the filter and step sizes is arranged as follows. Consider the width of the FPZ is 5.5 mm for the sample under study in Fig. 5. A sharp gradient of displacement is expected to be present at the middle of this region due to a possible macro-crack being developed there. In this case, the distance from the sharp displacement gradient to the boundary of the FPZ is 2.75 mm. Any smoothing scheme used on a distance larger than 2.75 mm inaccurately propagates the large gradient at the center of the FPZ beyond the actual boundary of the FPZ. The choices of thirteen pixels and five points respectively for step and filter sizes results in a smoothing distance of sixty-five pixels which is equivalent to about 1.625 mm, far below 2.75 mm. However, any filter size above eight points would make the smoothing distance to extend above 2.6 mm which is almost equal to the half of the FPZ width. Fig. 5b shows that the calculated width of the FPZ start to increase linearly above the filter size of about eight. This indicates that for such big filter sizes, the smoothing distance is larger than half of the FPZ, and therefore the calculated values of FPZ width are inaccurate, and the result of smoothing procedure.

According to this sensitivity analyses, it was concluded that a step size of thirteen pixels and filter size of five can provide accurate enough strain field for the evaluation of the FPZ size from strain localization. In fact, these parameters assure that the size of the FPZ obtained from strains are in very good agreement with the one obtained from displacement. It is noteworthy that the results in Fig. 5 also show that the FPZ width is not dependent on the load level above 60% of the peak-load. This observation agrees with similar findings in previous studies [49,60,63,72]. Note that the variation of the FPZ width obtained from displacements and strains at different loads is small (about 0.3 mm) compared to the actual value of the FPZ width which is about 5.5 mm.

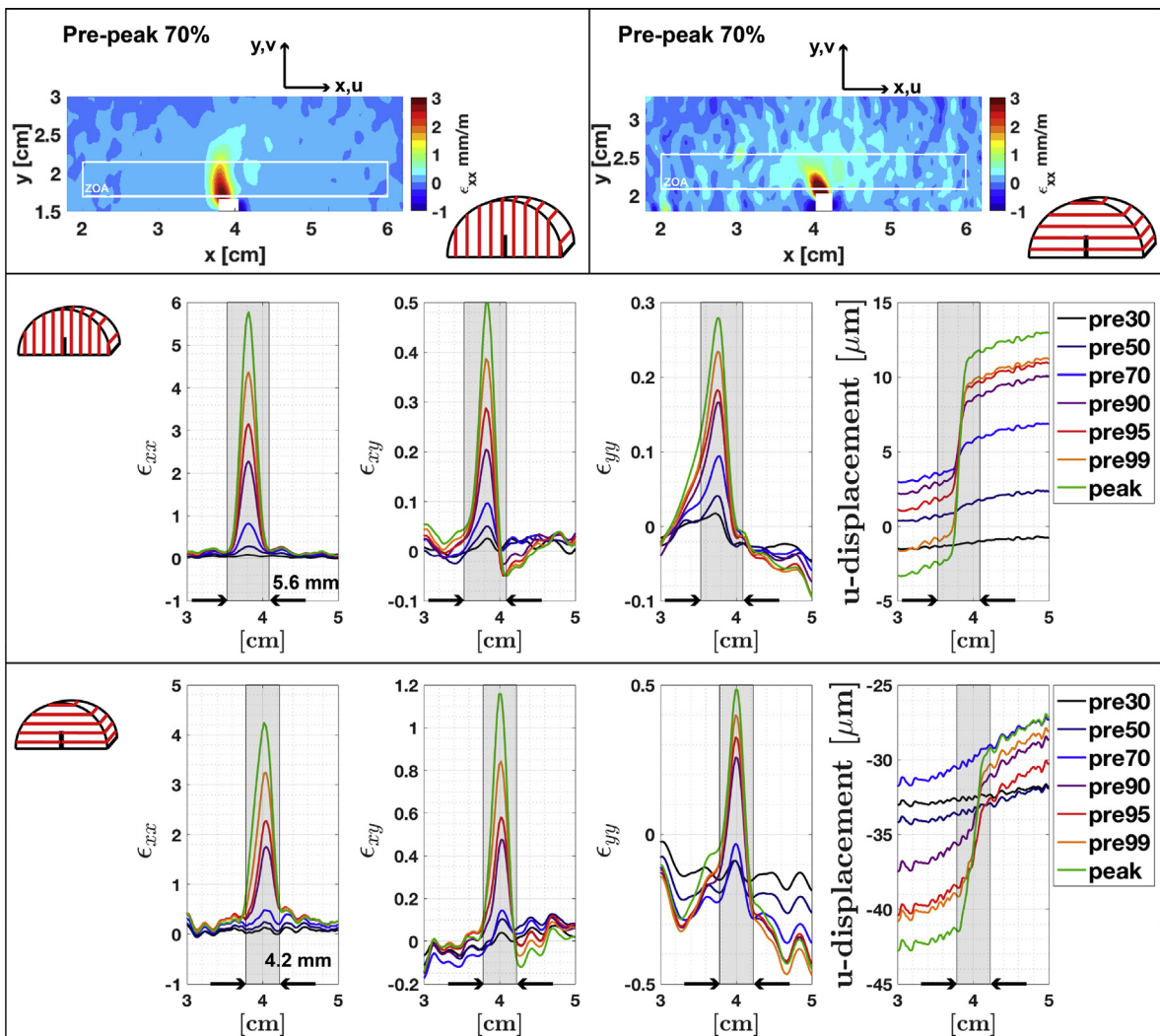


Fig. 7. The calculation of the FPZ width based on localization of strain components ϵ_{xx} , ϵ_{xy} , ϵ_{yy} , given in millistrain (mm/m) and the jump of displacement u for two end-member configurations of $\varphi = 0^\circ, 90^\circ$ at seven different loading stages prior to the peak load. The width of the FPZ corresponds to the width of the shaded region and measures $w = 5.6$ mm for $\varphi = 0^\circ$ and $w = 4.2$ mm for $\varphi = 90^\circ$. The width of the FPZ is picked using a zone of averaging (ZOA) at 70% of pre-peak load. According to the coordinate system shown, negative values of displacement imply movements to the left.

6.2. Shape of the fracture process zone

Fig. 6 shows the region with highly localized maximum principal strains ahead of the crack tip in the samples tested in two configurations $\varphi = 0^\circ, 90^\circ$. When the crack is oriented along foliation ($\varphi = 0^\circ$), almost all samples show the development of a semi-elliptical FPZ region. Although this is also the dominant shape in configuration $\varphi = 90^\circ$, the FPZ seems to show an angular deviation from the notch plane in some samples. The angular deviation of the FPZ can be attributed to the influence of micro-cracks oriented along the foliation, resulting in the tendency to change the direction of crack growth. This is the reason for having a more tortuous crack path observed in the post-mortem analyses. The semi-elliptical FPZ shape observed in our experiments agrees well with the results reported in many previous researches on the FPZ shape of quasi-brittle materials [46,47,49,52,54,62,70]. These results emphasize that butterfly-shaped FPZ obtained from analytical models are not accurate estimations of localized zones in quasi-brittle materials.

The overall conclusion from Fig. 6 is that the FPZ seems to be developed in a semi-elliptical region ahead of the crack tip. This finding is in very good agreement with the previous studies and also matches the strip-yield (Dugdale-Barenblatt) model. Fig. 6 shows a schematic representation of a semi-elliptical FPZ with the width of W and the length of L . These two length parameters seem to be independent, and are expected to be only material properties provided that the boundary of the FPZ is fully formed (no load dependency of the FPZ boundary) and the crack ligament is large enough (no boundary influence).

6.3. Size of the fracture process zone

Fig. 7 schematically shows the identification of the FPZ width from the strain localization and displacement jump in two specimens from different configurations. These results show the agreement of the FPZ width obtained from strains and displacements. All three components of strain show localization in the process zone, with the component normal to the crack plane, ϵ_{xx} , being an order of

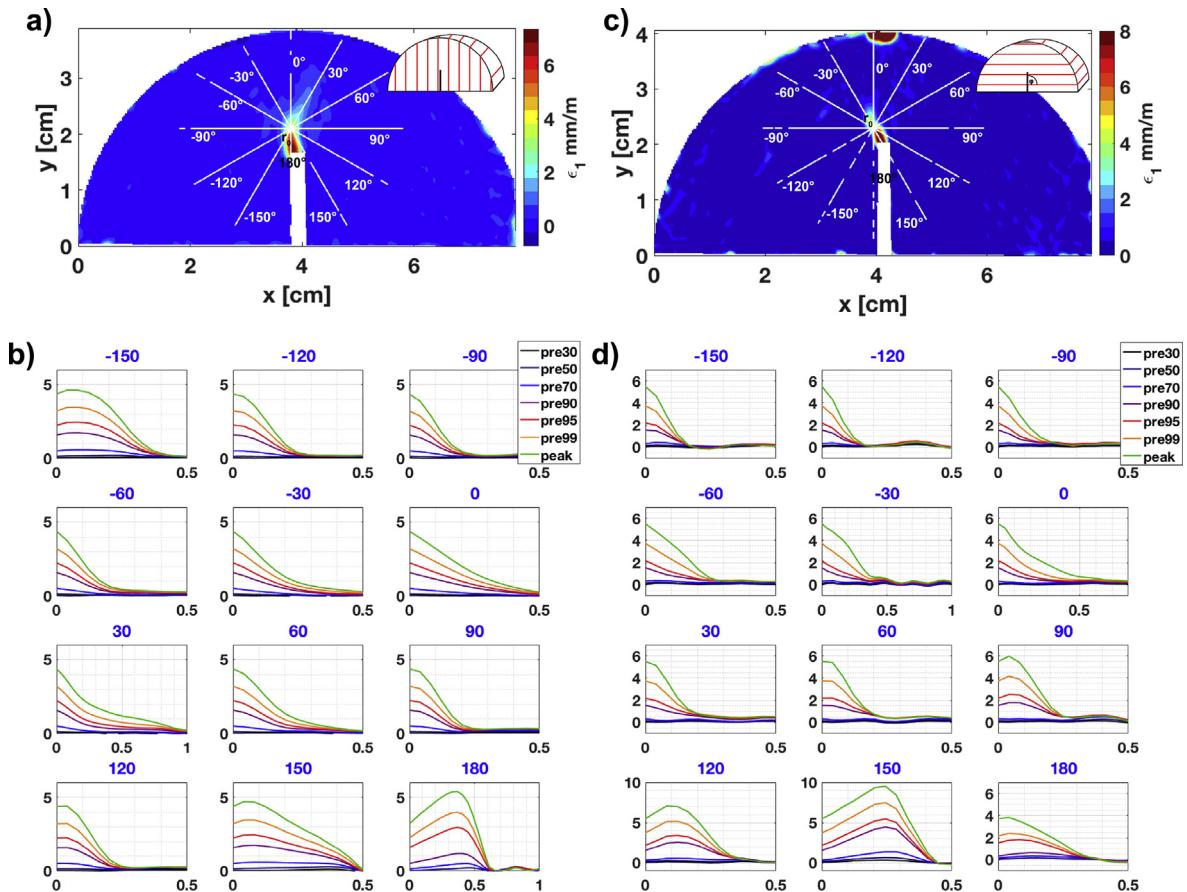


Fig. 8. (a, c) The contours of maximum principal strain ϵ_1 at peak load for two configurations $\varphi = 0^\circ, 90^\circ$. (b, d) The variation of ϵ_1 is given in millistrain (mm/m) along different radial paths originated from the point r_0 (white lines in (a) and (c)) for different pre-peak load levels from 30% up to the peak load. The blue colored numbers in the titles of the plots in (b) and (d) indicate the specific radial path shown in (a) and (c). The unit of the x-axis in (b) and (d) is cm. (For interpretation of the references to color in this figure legend, the reader is referred to the web version of this article.)

magnitude greater than the other two strain components. The width of the FPZ is picked using an zone of averaging (ZOA) at 70% of pre-peak load.

It is noteworthy that according to the values of tensile strength and Young’s moduli, a critical tensile strain of about 320 and 350 micro strains are obtained for the principal directions normal and parallel to the foliation. From the ϵ_{xx} plots in Fig. 7, it is seen that such values of critical strain are exceeded at a loading stage between 50% and 70% of the peak load. This loading level is in a very good agreement with the general belief that the development of inelastic deformation of quasi-brittle materials start at about 60–70% of the peak load [7].

Fig. 8 shows the variation of maximum principal strain ϵ_1 , along twelve paths oriented at different angles with respect to the crack plane. Localization of the maximum principal strain is a good indicator of the inelastic region i.e. the FPZ. Therefore, the plots in Fig. 8 can be used to define the boundary of the FPZ, whereby the length, width and shape of the FPZ are determined. At the peak load, the maximum principal strain reaches as high as 0.01 near the center of the FPZ (see Fig. 8d). This high strain reduces dramatically when approaching the FPZ boundary, with localized deformation vanishing completely along the FPZ boundary. The shapes of the strains along different paths at different loads have similar trends and show an onion skin structure, where the load increases the strain in the nonlinear region, but does not influences the strain values around the FPZ. This clearly shows the localization of strain in the FPZ by increasing load. It is seen from both contours and plots that the FPZ is bigger in the configuration $\varphi = 0^\circ$ than $\varphi = 90^\circ$, with the length to width ratio in both cases being $L/W \approx 2$.

Fig. 8 also shows that once the boundary of the FPZ is fully formed at about 70–90% of the peak load, the size of the FPZ is not load dependent anymore. However, this does not mean crack extension already starts at this load level or a cohesion-less crack is developed. The activation and coalescence of the micro-cracks can still continue within the FPZ, after the FPZ, or the region in which the energy dissipation occurs, has reached its ultimate size. Fakhimi et al. [92] reported the formation of cohesion-less crack surfaces before the peak load in their experiments. However, we can not confirm such traction-free surfaces being created before the peak load in our tests. This is because (1) the DIC measurement is only surface measurement and does not give any information with regard to the strains along the crack front, and (2) there is no tool to obtain tractions within the FPZ and high values of strain do not necessarily imply a cohesion-free surface.

Fig. 9 presents the measured values of the width (W) and the length (L) of the FPZ in two configurations $\varphi = 0^\circ, 90^\circ$. As it was previously mentioned, the boundary of the FPZ is developed earlier for $\varphi = 0^\circ$ than $\varphi = 90^\circ$. The data points for $\varphi = 90^\circ$ correspond to 90% pre-peak load, whereas the data point for $\varphi = 0^\circ$ are at 70% of the peak load. The results for twelve samples are given in this Figure as data points, with the mean values and the standard deviation (SD) are shown by red solid lines and dotted blue lines, respectively. For crack propagating along the foliation $\varphi = 0^\circ$, the mean values of the six tests measure $w = 5.4$ mm in width and $L = 10.84$ mm in length. For the configuration $\varphi = 90^\circ$, the mean values for the width and the length of the FPZ are 4.7 mm and 8.8 mm, respectively. The following remarks shall be noted:

- In both configurations $\varphi = 0^\circ$ and $\varphi = 90^\circ$, the average length to width ratio is $L/W \approx 2$.
- The fracture process zone is larger in size when the crack grows along the foliation compared to the case it propagates normal to the foliation. The ratio of the FPZ size in two directions is $L^{\varphi=0^\circ}/L^{\varphi=90^\circ} \approx W^{\varphi=0^\circ}/W^{\varphi=90^\circ} \approx 1.2$. This indicates that the fracture process zone is anisotropic in terms of size.

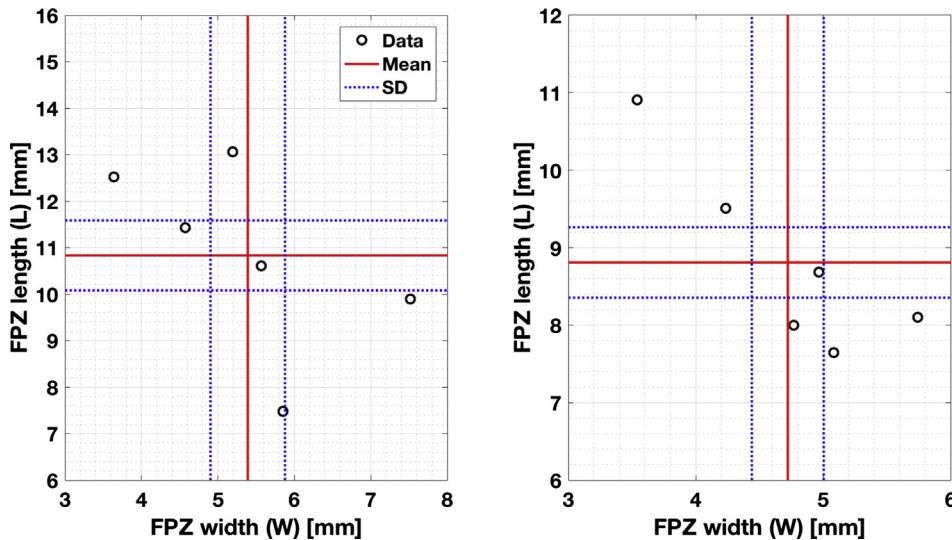


Fig. 9. The measured values for the FPZ width (W) and length (L) for two cases of $\varphi = 0^\circ$ and $\varphi = 90^\circ$. The mean values of the six tests are shown by red line, while the blue pointed line show the standard deviation. The results are taken from the fully formed FPZ, i.e. at 70% of pre-peak load for $\varphi = 0^\circ$ and 90% of pre-peak load for $\varphi = 90^\circ$. (For interpretation of the references to color in this figure legend, the reader is referred to the web version of this article.)

- The reason for a bigger FPZ along the foliation may be the preferred direction of micro-crack in such direction. Since the micro-cracks are oriented in the direction of crack growth, their activation and propagation can lead to a wider process zone.
- There is a negative correlation between the length and the width of the FPZ in both configurations. Both plots show that, the higher the FPZ width, the lower the FPZ length. One can explain this trend by considering that the energy dissipated via micro-cracking is a material property which drives the resistance of the material toward crack propagation. If one assumes that this energy is constant for a configuration, any increase in the FPZ length must be accompanied with a reduction in the FPZ width.
- The scatter of the FPZ width and length data can be attributed to the heterogeneous nature of rock. The mean values of the data are therefore considered as the representative values for these parameters.

It is noteworthy that the full development of the FPZ in rocks is a necessary condition for a reliable fracture toughness test. In both rocks and metals, the crack length and ligament are crucially important in order to allow the nonlinear zone to develop fully so that a representative fracture toughness can be measured. The specimen thickness requirement, however, seems to be of less importance in rock material compared to the metals. The reason is that the FPZ development in rocks is mainly due to tensile stresses, whereas the nonlinear plastic zone in metals mainly develops due to shear stresses. Therefore, while the size of the plastic zone depends significantly on the specimen thickness and out-of-plane stress, the FPZ size seems to be rather independent of whether the plane-stress or plane-strain condition holds [43]. Many experimental results obtained from different specimen types show that the measured fracture toughness is somewhat independent of the specimen thickness [93–99]. Therefore, the FPZ size obtained from the surface can technically show how the inelastic zone is developed within the solid, since a uniform FPZ is expected along the crack front.

Fig. 10 compares our results on the FPZ width and length with the results reported in previous research. Tarokh et al. [100] and Otsuka and Date [62] used concrete specimens with aggregate sizes up to 10 mm and obtained the FPZ length and width for various sample sizes. Backers [101] used sandstone specimens with grain sizes between 0.1 mm and 0.5 mm. Tarokh et al. [100] obtained the results from DIC experiments while Backers [101] and Otsuka and Date [62] conducted acoustic emission tests. This figure shows that the length to width ratio of the FPZ mainly varies between two and four. In addition, the size of the process zone increases with increasing the sample size, where the ratio L/W increases from two for small samples to about six for larger ones. Overall, the results characterize the FPZ of the quasi-brittle materials as a rather narrow semi-elliptical region.

7. Link between toughness, strength and the FPZ size

This section compares the experimental results on the FPZ size with the prediction of theoretical models. Let us consider a plane stress problem where one of the symmetry planes of the material is parallel to the symmetry plane of the model (normal to z -axis). According to the generalized Hooke’s law, the stress-strain relationship of an elastic anisotropic material within the plane follow

$$\begin{bmatrix} \epsilon_x \\ \epsilon_y \\ 2 \epsilon_{xy} \end{bmatrix} = \begin{bmatrix} S_{11} & S_{12} & S_{16} \\ S_{21} & S_{22} & S_{26} \\ S_{61} & S_{62} & S_{66} \end{bmatrix} \begin{bmatrix} \sigma_x \\ \sigma_y \\ \tau_{xy} \end{bmatrix} \tag{4}$$

where S_{ij} , $i, j = 1, 2, 6$ are the components for the compliance matrix. Considering a crack in the plane oriented along the x -axis, the stress field adjacent to the crack tip under mode I loading is given by Sih et al. [102]:

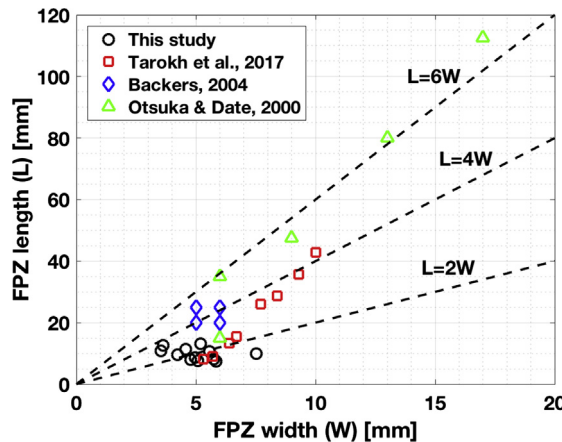


Fig. 10. The comparison of the width and length of the FPZ obtained from this study with the results given in three previous studies.

$$\begin{aligned}
 \sigma_x &= \frac{K_I}{\sqrt{2\pi r}} \Re \left[\frac{\mu_1 \mu_2}{\mu_1 - \mu_2} \left(\frac{\mu_2}{\sqrt{\cos\theta + \mu_2 \sin\theta}} - \frac{\mu_1}{\sqrt{\cos\theta + \mu_1 \sin\theta}} \right) \right] \\
 \sigma_y &= \frac{K_I}{\sqrt{2\pi r}} \Re \left[\frac{1}{\mu_1 - \mu_2} \left(\frac{\mu_1}{\sqrt{\cos\theta + \mu_2 \sin\theta}} - \frac{\mu_2}{\sqrt{\cos\theta + \mu_1 \sin\theta}} \right) \right] \\
 \tau_{xy} &= \frac{K_I}{\sqrt{2\pi r}} \Re \left[\frac{\mu_1 \mu_2}{\mu_1 - \mu_2} \left(\frac{1}{\sqrt{\cos\theta + \mu_1 \sin\theta}} - \frac{1}{\sqrt{\cos\theta + \mu_2 \sin\theta}} \right) \right]
 \end{aligned} \tag{5}$$

Here, r and θ are the polar coordinates of the point near the tip in the crack tip local coordinate system, \Re denotes the real part of complex numbers, and μ_1 and μ_2 are the roots of the characteristic equation, and are dependent on the component of the compliance matrix:

$$S_{11}\mu^4 - 2S_{16}\mu^3 + (2S_{12} + S_{66})\mu^2 - 2S_{26}\mu + S_{22} = 0 \tag{6}$$

This characteristic equation always has complex or pure imaginary roots which appear in conjugate pairs as $\mu_1, \bar{\mu}_1$ and $\mu_2, \bar{\mu}_2$. Let us now consider the stress variation along the crack ligament ($\theta = 0$):

$$\sigma_x = \frac{K_I}{\sqrt{2\pi r}} \Re[-\mu_1 \mu_2], \quad \sigma_y = \frac{K_I}{\sqrt{2\pi r}}, \quad \tau_{xy} = 0 \tag{7}$$

This equation shows the shear stress is zero along such path, and the stress component σ_y does not explicitly depend on the material properties. On the other hand, according to the solution by Sih et al. [102], the stress intensity factor for a central crack in an infinite anisotropic medium with remote stress of σ applied normal to the crack is given by $K_I = \sigma\sqrt{\pi a}$. This formula is identical to the one obtained for isotropic materials, which indicates that for a central crack, the material constants of the anisotropic medium do not influence σ_y along the crack ligament.

As it was mentioned in Section 3.1, the two main models used for the estimation of the size of the inelastic zone are the Irwin approach, and the strip-yield model with uniform and linear closing stresses along the FPZ. Both models use the stress component σ_y along the crack ligament to obtain estimations of the inelastic zone. Since this component of stress is not influenced by the material constants according to Eq. (7), both models can be readily extended to anisotropic materials without any modification. Table 8 presents the size of the process zone obtained from these two models in comparison with the experimental results. The theoretical prediction are based on the average measurements of fracture toughness and strength given in Tables 4 and 6. It is evident from the results that the Irwin model and the strip-yield model with uniform closing stress underestimate the length of the FPZ, whereas the strip-yield model with a linear closing stress overestimate the FPZ length.

These results give an interesting insight about the type of the micro-damaging that occurs in the FPZ. Since the experimental results give values in between the predictions of the strip-yield model with uniform and linear closing (cohesion) stress distribution, it is expected the cohesion stress in reality distributes nonlinearly with higher gradient near the crack tip as shown in Fig. 11. This means that the gradient of the micro-damaging and reduction of strength is much higher near the tip than towards the end of the process zone. These experimental results give supporting evidence to the fact that a non-linear distribution is more realistic than uniform or linear variation of the cohesion.

Let us now compare the ratio of the process zone obtained for the principal directions. Both models predict the same ratio of the FPZ length at two configurations $\varphi = 0^\circ$ and $\varphi = 90^\circ$ from:

$$\frac{L^{\varphi=0^\circ}}{L^{\varphi=90^\circ}} = \left(\frac{K_{Ic}^{\varphi=0^\circ}}{K_{Ic}^{\varphi=90^\circ}} \right)^2 \times \left(\frac{\sigma_t^{\varphi=90^\circ}}{\sigma_t^{\varphi=0^\circ}} \right)^2 \tag{8}$$

Using the measured values of fracture toughness and strength, one can predict the ratio of the FPZ length at two principal directions, and compares it with the experimental results of the FPZ size:

$$\left(\frac{L^{\varphi=0^\circ}}{L^{\varphi=90^\circ}} \right)_{\text{Model}} = 1.32, \quad \left(\frac{L^{\varphi=0^\circ}}{L^{\varphi=90^\circ}} \right)_{\text{Experiment}} = 1.23 \tag{9}$$

Eq. (9) shows that there is a very good agreement between the results obtained directly from the experiments, and the ones calculated from the models predicting the size of the process zone. This gives supporting evidence that the FPZ length is in fact

Table 8

The comparison of the FPZ length obtained from the experimental results with the theoretical models. Length values are in mm.

φ	Theoretical Models			Experiment
	Irwin $L_I = \frac{1}{\pi} \left(\frac{K_{Ic}}{\sigma_t} \right)^2$	Strip-yield uniform traction $L_{Su} = \frac{\pi}{8} \left(\frac{K_{Ic}}{\sigma_t} \right)^2$	Strip-yield linear traction $L_{Sl} = \frac{9\pi}{32} \left(\frac{K_{Ic}}{\sigma_t} \right)^2$	
0°	5.4	6.6	14.9	10.8
90°	4.1	5	11.3	8.8
Ratio		1.32		1.23

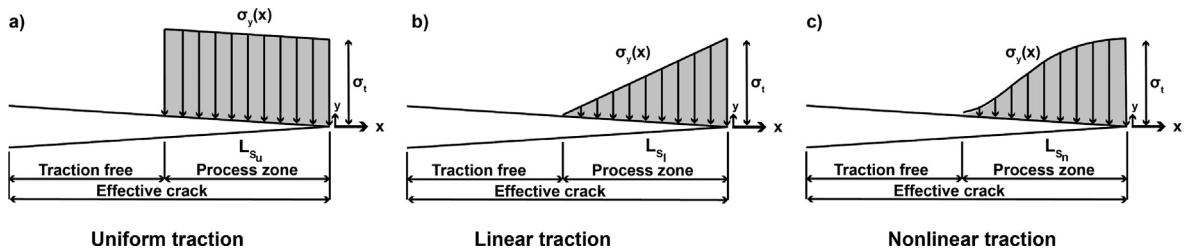


Fig. 11. Schematic of models with uniform, linear and nonlinear distributions of cohesion stress along the FPZ. A cohesive model based on the nonlinear distribution matches the experimental results better than the uniform and linear types.

proportional to the square of the fracture toughness to strength ratio: $L \propto (K_{Ic}/\sigma_t)^2$. The proportional constant depends on the details of the damaging processes in the FPZ.

It is worth noting that the large FPZ size obtained for granodiorite samples in this study demonstrates the development of a large nonlinear zone ahead of the crack tip. One important implication of this finding is that the LEFM concept may not be applicable to small samples since a large portion of the sample deforms nonlinearly. The tests conducted in this research follow the size requirements of the ISRM suggested method [11]: $D \geq 2(K_{Ic}/\sigma_t)^2$. Based on the measured strength and fracture toughness values, the requirement for the minimum diameter of the samples are $D = 34$ mm for $\phi = 0^\circ$ and $D = 26$ mm for $\phi = 90^\circ$, which is significantly lower than the diameter of the samples $D = 82.9$ mm. The suggested size requirement assures the full development of the FPZ in order to obtain reliable values of the fracture toughness. This raises an important question: Is the LEFM valid for the entire range of sizes that are acceptable based on the size requirement of the ISRM suggested method? Further research is welcome to answer this question.

In addition, such big FPZ size also questions one-parameter fracture propagation criteria to be applicable for such rocks. These criteria are formulated based on only singular terms of the crack tip asymptotic fields, and the higher order terms are ignored based on an assumption of small process zones. However, many experimental studies have demonstrated the significance of the higher order terms to be included in the fracture growth criteria for rocks with large process zones [44,45,103,104]. Ayatollahi and Akbaridoost [105], and Akbaridoost and Ayatollahi [106] explained the dependency of the fracture toughness on the specimen size using a multi-parameter fracture criterion.

It is important to emphasize that the tensile strength results in this research are obtained indirectly from the Brazilian disk test. Experimental results show that the Brazilian test overestimates the true tensile strength, perhaps due to the applied compressive stress parallel to the loading axis in the BD test. Nevertheless, the Brazilian tensile strength still gives reasonable estimates of the true tensile strength of rock [26]. We should note that the tensile strength of the rock material in the FPZ may also in essence differ from the true tensile strength of rock. This is because the rock material in the process zone is under a biaxial state of the stress and not a uniaxial one. In fact, the stress component parallel to the crack, called T-stress, is negative for the SCB specimen configuration used in this study [107]. Hence, the nature of the failures in the SCB and BD are in fact similar in the sense that a compressive stress is applied parallel to the failure plane. In this case, strength obtained from the BD test may be more representative of the failure in the FPZ rather than the true tensile strength obtained from direct tests.

8. Conclusions

- Experimental results of Grimsel Granodiorite samples show anisotropy ratios of 2.27 and 2.61 for fracture toughness and Brazilian tensile strength, respectively. This indicates that the resistance against material failure is significantly higher in the direction normal to the foliation plane compared to the direction of the foliation plane.
- The post-mortem analyses shows significant difference of fracture path and surface characteristics between the two principal directions. The fracture surface shows higher roughness and more deviation from the expected path in the direction normal to the foliation compared to the direction along the foliation.
- The averaging scheme proposed for the measurement of the FPZ from DIC results calculates the width of the FPZ accurately, whereby the results from the strain and displacement fields match very well.
- The DIC results confirms the development of a semi-elliptical fracture process zone with an average length to width ratio of about two for both principal directions. These results agree well with the available results in the literature which suggest a ratio between two to four.
- The boundary of the FPZ fully forms at about 70% of the pre-peak load for crack oriented along the foliation plane, while about 90% of pre-peak load is required for crack oriented normal to the foliation. Above these load levels and before the crack extension occurs, micro-crack activation and coalescence is constrained within the boundary of the FPZ.
- Theoretical models of Irwin and strip-yield with uniform cohesion stress distribution underestimate the length of the FPZ. These models are based on the plastic deformation near the crack tip, and one can expect they underestimate the length of the FPZ for quasi-brittle materials in which the inelastic deformation is strongly dominated by damage rather than plasticity. On the other hand, it is found the strip-yield model with a linear cohesion stress distribution overestimate the length of the process zone. The experimental results give supporting evidence to the fact that a nonlinear cohesion stress distribution provides a more accurate

cohesive model that agrees better with the experimental results.

- The ratio of the FPZ length in two principal directions agrees very well with the theoretical predictions. This gives supporting evidence to the proportionality of the FPZ length with respect to the square of fracture toughness to tensile strength: $L \propto (K_{Ic}/\sigma_t)^2$, where the proportionality constant can be obtained from theoretical models or experiments.

Acknowledgement

The ISC is a project of the Deep Underground Laboratory at ETH Zurich, established by the Swiss Competence Center for Energy Research-Supply of Electricity (SCCER-SoE) with the support of the Swiss Commission for Technology and Innovation (CTI). Funding for the ISC project was provided by the ETH Foundation with grants from Shell and EWZ and by the Swiss Federal Office of Energy through a P&D grant. Nathan Dutler is supported by SNF Grant No. 200021_165677. The DIC system from the Composite Materials and Adaptive Structures laboratory was acquired through the SNF R'Equip Grant No. 206021_150729. The authors like to thank Claudio Madonna for using the Rock Deformation Laboratory and Nils Knornschild, Thomas Mörgele and Thomas Good for their help for equipments, sample preparation and testing.

References

- [1] Amann F, Gischig V, Evans K, Doetsch J, Jalali R, Valley B, et al. The seismo-hydronechanical behavior during deep geothermal reservoir stimulations: open questions tackled in a decameter-scale in situ stimulation experiment. *Solid Earth* 2018;9(1):115–37.
- [2] Gischig V, Doetsch J, Maurer H, Krietsch H, Amann F, Frederick Evans K, et al. On the link between stress field and small-scale hydraulic fracture growth in anisotropic rock derived from microseismicity. *Solid Earth* 2018;9(1):39–61.
- [3] Jalali M, Gischig V, Doetsch J, Naf R, Krietsch H, Klepikova M, et al. Transmissivity changes and microseismicity induced by smallscale hydraulic fracturing tests in crystalline rock. *Geophys Res Lett* 2018;45:2265–73.
- [4] Olgaard DL, Brace WF. The microstructure of gouge from a mining-induced seismic shear zone. *Int J Rock Mech Min Sci* 1983;20(1):11–9.
- [5] Hoagland RG, Hahn GT, Rosenfield AR. Influence of microstructure on fracture propagation in rock. *Rock Mech* 1973;5(2):77–106.
- [6] Anders MH, Laubach SE, Scholz CH. Microfractures: a review. *J Struct Geol* 2014;69:377–94.
- [7] Whittaker BN, Singh RN, Sun G. Rock fracture mechanics: principles, design and applications. *Rock Fract Mech: Principles Des Appl*; 1992.
- [8] Bearman R. The use of the point load test for the rapid estimation of Mode I fracture toughness. *Int J Rock Mech Min Sci* 1999;36(2):257–63.
- [9] Uchtlerlony F. Suggested methods for determining the fracture toughness of rock. *Int J Rock Mech Min Sci Geomech Abstr Geomech Abstr* 1988;25(2):71–96.
- [10] Fowell RJ. Suggested method for determining mode I fracture toughness using Cracked Chevron Notched Brazilian Disc (CCNBD) specimens. *Int J Rock Mech Min Sci Geomech Abstr* 1995;32(1):57–64.
- [11] Kuruppu MD, Obara Y, Ayatollahi MR, Chong KP, Funatsu T. ISRM-suggested method for determining the mode I static fracture toughness using semi-circular bend specimen. *Rock Mech Rock Eng* 2014;47(1):267–74.
- [12] Dwivedi R, Soni A, Goel R, Dube A. Fracture toughness of rocks under sub-zero temperature conditions. *Int J Rock Mech Min Sci* 2000;37(8):1267–75.
- [13] Iqbal MJ, Mohanty B. Experimental calibration of ISRM suggested fracture toughness measurement techniques in selected brittle rocks. *Rock Mech Rock Eng* 2007;40(5):453–75.
- [14] Kataoka M, Yoshioka S, Cho S-H, Soucek K, Vavro L, Obara Y. Estimation of fracture toughness of sandstone by three testing methods. In: *Vietrock2015 an ISRM specialized conference (March)*; 2015b.
- [15] Krishnan G, Zhao X, Zaman M, Roegiers J-C. Fracture toughness of a soft sandstone. *Int J Rock Mech Min Sci* 1998;35(6):695–710.
- [16] Ke CC, Chen CS, Tu CH. Determination of fracture toughness of anisotropic rocks by boundary element method. *Rock Mech. Rock Eng* 2008;41(4):509–38.
- [17] Kataoka M, Obara Y. Estimation of fracture toughness of anisotropic rocks by SCB test and visualization of fracture by means of X-ray CT. *Test* 2012;667–70.
- [18] Kataoka M, Obara Y, Kuruppu M. Estimation of fracture toughness of anisotropic rocks by semi-circular bend (SCB) tests under water vapor pressure. *Rock Mech Rock Eng* 2015;48(4):1353–67.
- [19] Nasser MHB, Mohanty B. Fracture toughness anisotropy in granitic rocks. *Int J Rock Mech Min Sci* 2008;45(2):167–93.
- [20] Chandler MR, Meredith PG, Brantut N, Crawford BR. Fracture toughness anisotropy in shale. *J Geophys Res: Solid Earth* 2016;121:1706–29.
- [21] Chandler MR, Meredith PG, Brantut N, Crawford BR. Effect of temperature on the fracture toughness of anisotropic shale and other rocks. *Geological Society, London, Special Publications, SP454.6*; 2017.
- [22] Funatsu T, Takashi T, Kuruppu M. Effect of anisotropy on fracture toughness of sandstone by SCB specimen. In: *ISRM regional symposium – 7th Asian rock mechanics symposium, ISRM-ARMS7–2012–041*; 2012.
- [23] Nasser MHB, Tatone BSA, Grasselli G, Young RP. Fracture toughness and fracture roughness interrelationship in thermally treated westerly granite. *Pure Appl Geophys* 2009;166(5–7):801–22.
- [24] Nasser MHB, Grasselli G, Mohanty B. Fracture toughness and fracture roughness in anisotropic granitic rocks. *Rock Mech Rock Eng* 2010;43(4):403–15.
- [25] Li D, Wong LNY. The brazilian disc test for rock mechanics applications: review and new insights. *Rock Mech Rock Eng* 2013;46(2):269–87.
- [26] Perras MA, Diederichs MS. A review of the tensile strength of rock: concepts and testing. *Geotech Geol Eng* 2014;32(2):525–46.
- [27] Hondros G. The evaluation of Poisson's ratio and the modulus of materials of a low tensile resistance by the Brazilian (indirect tensile) test with particular reference to concrete. *Aust J Appl Sci* 1959;10(3):243–68.
- [28] Bieniawski Z, Bernede M. Suggested methods for determining the uniaxial compressive strength and deformability of rock materials. *Int J Rock Mech Min Sci Geomech Abstr* 1979;16(2):137–40.
- [29] ASTM. Standard test method for direct tensile strength of intact rock core specimens. *ASTM International D 3967-08*; 2008.
- [30] Chen C-s, Pan E, Amadei B. Determination of deformability and tensile strength of anisotropic rock using Brazilian Tests. *Int J Rock Mech Min Sci Geomech Abstr Geomech Abstr* 1998;35(1):43–61.
- [31] Exadaktylos GE, Kakkis KN. Applications of an explicit solution for the transversely isotropic circular disc compressed diametrically. *Int J Rock Mech Min Sci* 2001;38(2):227–43.
- [32] Claesson J, Bohloli B. Brazilian test: stress field and tensile strength of anisotropic rocks using an analytical solution. *Int J Rock Mech Min Sci* 2002;39(8):991–1004.
- [33] Lekhnitskiy SG. Anisotropic plates. *Anisotropic Plates* 1969:477.
- [34] Barla G, Innaurato N. Indirect tensile testing of anisotropic rocks. *Rock Mech* 1973;5(4):215–30.
- [35] Tavallali A, Vervoort A. Behaviour of layered sandstone under Brazilian test conditions: layer orientation and shape effects. *Int J Rock Mech Min Sci* 2010;47:313–22.
- [36] Vervoort A, Min K-B, Konietzky H, Cho J-W, Debecker B, Dinh Q-D, et al. Failure of transversely isotropic rock under Brazilian test conditions. *Int J Rock Mech Min Sci* 2014;70:343–52.
- [37] Khanlari G, Rafiei B, Abdilor Y. Evaluation of strength anisotropy and failure modes of laminated sandstones. *Arab J Geosci* 2015;8(5):3089–102.
- [38] Wild KM, Wymann LP, Zimmer S, Thoeny R, Amann F. Water retention characteristics and state-dependent mechanical and petro-physical properties of a clay shale. *Rock Mech Rock Eng* 2015;48(2):427–39.

- [39] Irwin GR. Plastic zone near a crack and fracture toughness. In: *Sagamore research conference proceedings*, vol. 4; 1961. p. 63–78.
- [40] Barenblatt GI. The formation of equilibrium cracks during brittle fracture. General ideas and hypotheses. Axially-symmetric cracks. *J Appl Math Mech* 1959;23(3):622–36.
- [41] Dugdale D. Yielding of steel sheets containing slits. *J Mech Phys Solids* 1960;8(2):100–4.
- [42] Labuz J, Shah S, Dowding C. Experimental analysis of crack propagation in granite. *Int J Rock Mech Min Sci Geomech Abstr Geomech Abstr* 1985;22(2):85–98.
- [43] Schmidt RA. A microcrack model and its significance to hydraulic fracturing and fracture toughness testing. In: *The 21st U.S. symposium on rock mechanics (USRMS)*, ARMA–80–0581; 1980.
- [44] Smith DJ, Ayatollahi MR, Pavier MJ. The role of T-stress in brittle fracture for linear elastic materials under mixed-mode loading. *Fatigue Fract Eng Mater Struct* 2001;24(2):137–50.
- [45] Aliha MR, Ayatollah MR, Smith DJ, Pavier MJ. Geometry and size effects on fracture trajectory in a limestone rock under mixed mode loading. *Eng Fract Mech* 2010;77(11):2200–12.
- [46] Zietlow WK, Labuz JF. Measurement of the intrinsic process zone in rock using acoustic emission. *Int J Rock Mech Min Sci* 1998;35(3):291–9.
- [47] Chengyong W, Peidat L, Rongshengt H. Study of the fracture process zone in rock by laser speckle interferometry. *Int J Rock Mech Min Sci Geomech Abstr* 1990;27(1):65–9.
- [48] Guo ZK, Kobayashi AS, Hawkins NM. Further studies on fracture process zone for mode I concrete fracture. *Eng Fract Mech* 1993;46(6):1041–9.
- [49] Wu Z, Rong H, Zheng J, Xu F, Dong W. An experimental investigation on the FPZ properties in concrete using digital image correlation technique. *Eng Fract Mech* 2011;78(17):2978–90.
- [50] Lin Q, Labuz JF. Fracture of sandstone characterized by digital image correlation. *Int J Rock Mech Min Sci* 2013;60:235–45.
- [51] Lin Q, Yuan H, Biolzi L, Labuz JF. Opening and mixed mode fracture processes in a quasi-brittle material via digital imaging. *Eng Fract Mech* 2014;131:176–93.
- [52] Backers T, Stanchits S, Dresen G. Tensile fracture propagation and acoustic emission activity in sandstone: the effect of loading rate. *Int J Rock Mech Min Sci* 2005;42(7-8 SPEC. ISS.):1094–101.
- [53] Lin Q, Fakhimi A, Haggerty M, Labuz JF. Initiation of tensile and mixed-mode fracture in sandstone. *Int J Rock Mech Min Sci* 2009;46(3):489–97.
- [54] Swanson PL, Spetzler H. Ultrasonic probing of the fracture process zone in rock using surface waves. In: *The 25th US symposium on rock mechanics (USRMS)*; 1984.
- [55] Labuz JF, Shah SP, Dowding CH. The fracture process zone in granite: evidence and effect. *Int J Rock Mech Min Sci Geomech Abstr Geomech Abstr* 1987;24(4):235–46.
- [56] Zang A, Wagner F. Fracture process zone in granite. *J Geophys Res* 2000;105(B10):23651–61.
- [57] Brooks Z, Ulm F-J, Einstein HH. Role of microstructure size in fracture process zone development of marble. *American Rock Mechanics Association*; 2012.
- [58] Brooks Z, Ulm FJ, Einstein HH. Environmental scanning electron microscopy (ESEM) and nanoindentation investigation of the crack tip process zone in marble. *Acta Geotech* 2013;8(3):223–45.
- [59] Brooks Z. *Fracture process zone: microstructure and nanomechanics in quasi-brittle materials [PhD Thesis]*; 2013. p. 355.
- [60] Alam SY, Saliba J, Loukili A. Fracture examination in concrete through combined digital image correlation and acoustic emission techniques. *Constr Build Mater* 2014;69:232–42.
- [61] Alam SY, Loukili A, Grondin F, Rozière E. Use of the digital image correlation and acoustic emission technique to study the effect of structural size on cracking of reinforced concrete. *Eng Fract Mech* 2015;143:17–31.
- [62] Otsuka K, Date H. Fracture process zone in concrete tension specimen. *Eng Fract Mech* 2000;65(2–3):111–31.
- [63] Skarżyński L, Tejchman J. Experimental investigations of fracture process using DIC in plain and reinforced concrete beams under bending. *Strain* 2013;49(6):521–43.
- [64] Nasser MHB, Mohanty B, Robin PYF. Characterization of microstructures and fracture toughness in five granitic rocks. *Int J Rock Mech Min Sci* 2005;42(3):450–60.
- [65] Scholz CH, Dawers NH, Yu J-Z, Anders MH, Cowie PA. Fault growth and fault scaling laws: preliminary results. *J Geophys Res: Solid Earth* 1993;98(B12):21951–61.
- [66] Vermilye JM, Scholz CH. The process zone: a microstructural view of fault growth. *J Geophys Res* 1998;103:12223–37.
- [67] Janssen C, Wagner F, Zang A, Dresen G. Fracture process zone in granite: a microstructural analysis. *Int J Earth Sci* 2001;90(1):46–59.
- [68] Nasser MHB, Mohanty B, Young RP. Fracture toughness measurements and acoustic emission activity in brittle rocks. *Pure Appl Geophys* 2006;163(5–6):917–45.
- [69] Faulkner DR, Mitchell TM, Jensen E, Cembrano J. Scaling of fault damage zones with displacement and the implications for fault growth processes. *J Geophys Res: Solid Earth* 2011;116(5):1–11.
- [70] Skarżyński A, Szyroka E, Tejchman J. Measurements and calculations of the width of the fracture process zones on the surface of notched concrete beams. *Strain* 2011;47:319–32.
- [71] Dong W, Wu Z, Zhou X, Dong L, Kastiukas G. FPZ evolution of mixed mode fracture in concrete: experimental and numerical. *Eng Fail Anal* 2017;75:54–70.
- [72] Skarżyński, Kozicki J, Tejchman J. Application of DIC technique to concrete-study on objectivity of measured surface displacements. *Exp Mech* 2013;53(9):1545–59.
- [73] Dong W, Wu Z, Zhou X, Wang N, Kastiukas G. An experimental study on crack propagation at rock-concrete interface using digital image correlation technique. *Eng Fract Mech* 2017;171:50–63.
- [74] Corr D, Accardi M, Graham-Brady L, Shah S. Digital image correlation analysis of interfacial debonding properties and fracture behavior in concrete. *Eng Fract Mech* 2007;74(1–2):109–21.
- [75] Enfedaque A, Gálvez JC, Suárez F. Analysis of fracture tests of glass fibre reinforced cement (GRC) using digital image correlation. *Constr Build Mater* 2015;75:472–87.
- [76] Krietsch H, Doetsch J, Dutler NO, Jalali M, Gischig VS, Loew S, et al. Comprehensive geological data of a fractured crystalline rock mass analog for hydraulic stimulation experiments. *Nat Sci Data* 2018. [under review].
- [77] Keusen H, Ganguin J, Schuler P, Buletti M. *Geologie. Tech. Rep. NTB87-14, Nagra, Wettingen*; 1989.
- [78] Schaltegger U. *Geochemische und isotopengeochemische Untersuchungen am zentralen Aaregranit und seinen assoziierten Gesteinen zwischen Aare und Reuss (Aaremassiv, Schweiz) [Ph.D. thesis]. Diss. phil.-nat. Bern, 1989, Bern*; 1989.
- [79] Schneberger R, de La Varga M, Egli D, Berger A, Kober F, Wellmann F, et al. Methods and uncertainty estimations of 3-d structural modelling in crystalline rocks: a case study. *Solid Earth* 2017;8(5):987–1002.
- [80] Challandes N, Marquer D, Villa IM. P-T-t modelling, fluid circulation, and 39Ar-40Ar and Rb-Sr mica ages in the Aar Massif shear zones (Swiss Alps). *Swiss J Geosci* 2008;101(2):269–88.
- [81] Dambly L, Nejati M, Vogler D, Saar MO. On the direct measurement of the shear moduli in transversely isotropic rocks using the uniaxial compression test. *Int J Rock Mech Min Sci* 2018. [under review].
- [82] Nejati M, Dambly L, Saar MO. Measurement of elastic constants of transversely isotropic rocks from a single uniaxial compression test. *Rock Mech Rock Eng* 2018. [under review].
- [83] Correlated Solutions, Inc. *Vic-3D Digital Imager Correlation Version 7.2.6*. Irmo, Columbia, USA; 2016.
- [84] The MathWorks Inc. *Matlab version 9.3.0 (R2017b)*. Natick, Massachusetts, USA; 2017.
- [85] ABAQUS/CAE. *Abaqus 6.14 Online Documentation*. Providence, RI, USA: Dassault Systemes Simulia Corp.; 2014.
- [86] Shih CF, Asaro RJ. Elastic-plastic analysis of cracks on bimaterial interfaces: Part I. Small scale yielding. *J Appl Mech* 1988;55:299–316.
- [87] Nejati M, Paluszny A, Zimmerman RW. A disk-shaped domain integral method for the computation of stress intensity factors using tetrahedral meshes. *Int J Solids Struct* 2015;230–51.
- [88] Wang SS, Yau JF, Corten HT. A mixed-mode crack analysis of rectilinear anisotropic solids using conservation laws of elasticity. *Int J Fract* 1980;16(3):247–59.

- [89] Banks-sills L, Hershkovitz I, Wawrzynek PA, Eliasi R, Ingraffea AR. Methods for calculating stress intensity factors in anisotropic materials: Part I $z = 0$ is a symmetric plane. *Eng Fract Mech* 2005;72:2328–58.
- [90] Banks-sills L, Wawrzynek PA, Carter B, Ingraffea AR, Hershkovitz I. Methods for calculating stress intensity factors in anisotropic materials: Part II arbitrary geometry. *Eng Fract Mech* 2007;74:1293–307.
- [91] Saouma VE, Ayari ML, Leavell DA. Mixed mode crack propagation in homogeneous anisotropic solids. *Eng Fract Mech* 1987;27(2):171–84.
- [92] Fakhimi A, Tarokh A, Labuz JF. Cohesionless crack at peak load in a quasi-brittle material. *Eng Fract Mech* 2017;179:272–7.
- [93] Schmidt RA, Lutz TJ. K_{IC} and J_{IC} of westerly granite-effects of thickness and in-plane dimensions. *ASTM Int* 1979:166–82.
- [94] Laqueche H, Rousseau A, Valentin G. Crack propagation under mode I and II loading in slate schist. *Int J Rock Mech Min Sci Geomech Abstr Geomech Abstr* 1986;23(5):347–54.
- [95] Kobayashi R, Matsuki K, Otsuka N. Size effect in the fracture toughness of Ogino tuff. *Int J Rock Mech Min Sci Geomech Abstr Geomech Abstr* 1986;23(1):13–8.
- [96] Singh RN, Sun G. A numerical and experimental investigation for determining fracture toughness of Welsh limestone. *Min Sci Technol* 1990;10:61–70.
- [97] Haberfield CM, Johnston IW. Determination of the fracture toughness of a saturated soft rock. *Can Geotech J* 1990;27:276–84.
- [98] Lim IL, Johnston IW, Choi SK, Boland JN. Fracture testing of a soft rock with semi-circular specimens under three-point bending. Part 2—mixed-mode. *Int J Rock Mech Min Sci Geomech Abstr Geomech Abstr* 1994;31(3):185–97.
- [99] Khan K, Al-Shayea NA. Effect of specimen geometry and testing method on mixed mode I-II fracture toughness of a limestone rock from Saudi Arabia. *Rock Mech Rock Eng* 2000;33(3):179–206.
- [100] Tarokh A, Makhnenko RY, Fakhimi A, Labuz JF. Scaling of the fracture process zone in rock. *Int J Fract* 2017;204(2):191–204.
- [101] Backers T. Fracture toughness determination and micromechanics of rock under mode I and mode II loading [PhD Thesis]. Germany: Geoforschungszentrum; 2004.
- [102] Sih GC, Paris PC, Irwin GR. On cracks in rectilinearly anisotropic bodies. *Int J Fract Mech* 1965;1(3):189–203.
- [103] Ayatollahi MR, Aliha MR. On the use of Brazilian disc specimen for calculating mixed mode I-II fracture toughness of rock materials. *Eng Fract Mech* 2008;75(16):4631–41.
- [104] Aliha MR, Sistaninia M, Smith DJ, Pavier MJ, Ayatollahi MR. Geometry effects and statistical analysis of mode I fracture in giting limestone. *Int J Rock Mech Min Sci* 2012;51:128–35. <https://doi.org/10.1016/j.ijrmms.2012.01.017>.
- [105] Ayatollahi MR, Akbaridoost J. Size effects on fracture toughness of quasi-brittle materials – a new approach. *Eng Fract Mech* 2012;92:89–100.
- [106] Akbaridoost J, Ayatollahi MR. Experimental analysis of mixed mode crack propagation in brittle rocks: the effect of non-singular terms. *Eng Fract Mech* 2014;129:77–89.
- [107] Ayatollahi MR, Aliha MR. Wide range data for crack tip parameters in two disc-type specimens under mixed mode loading. *Comput Mater Sci* 2007;38(4):660–70.
- [108] Nasser MHB, Rezanezhad F, Young RP. Analysis of fracture damage zone in anisotropic granitic rock using 3D X-ray CT scanning techniques. *Int J Fract* 2011;168(1):1–13.
- [109] Dai F, Xia K, Nasser MHB. Micromechanical model for the rate dependence of the fracture toughness anisotropy of Barre granite. *Int J Rock Mech Min Sci* 2013;63:113–21.
- [110] Lee HP, Olson JE, Holder J, Gale JFW, Myers RD. The interaction of propagating opening mode fractures with preexisting discontinuities in shale. *J Geophys Res: Solid Earth* 2015;120:169–81.